Ground Motions for Induced Earthquakes in Oklahoma

by Emrah Yenier, Gail M. Atkinson, and Danielle F. Sumy

Abstract   We examine ground motions for a sequence of earthquakes in Oklahoma, where assessment of hazard contributions from induced seismicity is of particular interest. We aim to empirically calibrate a model-driven equation that was derived for central and eastern North America (CENA), so that it will match the observed ground motions of the 2011 Prague, Oklahoma, sequence. We first show that ground motions in Oklahoma decay at a rate similar to the average attenuation observed in the stable continental region of CENA. We then search for any needed adjustments to the CENA source model to match ground motions from the induced seismicity sequence that occurred near Prague in 2011. An interesting feature noted in the ground-motion analysis is that the stress parameters ($\Delta\sigma$) for the Prague mainshock events ($\mathbf{M} \geq 5$) are notably higher than those for aftershocks. Moreover, the stress parameter that characterizes the high-frequency ground-motion decays in both time and space relative to the three largest events. The largest events in the Prague sequence have similar source parameters to natural CENA events of the same magnitude and focal depth, but their aftershocks have weaker motions.

Introduction

Seismic activity in Oklahoma has substantially increased within the last decade, surpassing the annual rate of moment magnitude $\mathbf{M} > 3.0$ events in California in 2014 on a per area basis. Llenos and Michael (2013) indicate that the elevated activity in Oklahoma is not a result of random rate fluctuations and can only be explained by a fundamental change in the underlying triggering properties of earthquakes. It is not generally feasible or useful to definitively classify (with 100% certainty) earthquakes as natural, directly induced, or indirectly triggered on an individual basis, but most of the events are believed to be related to changes in stress conditions resulting from large-scale wastewater injection. Thus most of the increased seismicity is considered to be induced by anthropogenic activities. (We do not attempt to distinguish between events that are directly induced versus those that may, in turn, be triggered by directly induced events. Such a distinction is not warranted for hazard or ground-motion applications, as will be discussed further).

On 5 November 2011, an $\mathbf{M}$ 5.0 earthquake occurred in close proximity to active disposal wells near the town of Prague, Oklahoma. This event initiated a sequence of small-to-moderate earthquakes on the complex Wilzetta fault system in the region, including the study events as shown in Figure 1. The $\mathbf{M}$ 5.0 event was followed by an $\mathbf{M}$ 5.7 earthquake the next day, which created ground shaking up to intensity VIII and caused structural damage in the epicentral region (Ellsworth 2013; Keranen *et al.*, 2013). On 8 November another $\mathbf{M}$ 5.0 earthquake occurred, less than 2 km west of the $\mathbf{M}$ 5.7 event. All three $\mathbf{M} \geq 5.0$ earthquakes exhibit strike-slip faulting with orientations consistent with rupture on three separate focal planes. Keranen *et al.* (2013) and Sumy *et al.* (2014) suggested that different parts of the Wilzetta fault system were activated in a succession of ruptures of three neighboring fault segments. Keranen *et al.* (2013) related the first $\mathbf{M}$ 5.0 event to the buildup of pore pressure due to fluid injection in the area for two decades, and Sumy *et al.* (2014) inferred that this event triggered the following $\mathbf{M}$ 5.7 and 5.0 earthquakes, in a cascading earthquake sequence. (The values for magnitude for the three mainshocks are taken from the Global Centroid Moment Tensor [CMT] catalog; see Data and Resources.) Because the three largest events occurred on three different fault segments, with differing orientations, they are considered as three distinct mainshock events within the sequence (Sumy *et al.*, 2014).

The 2011 Prague sequence and growing seismicity rate in Oklahoma have raised concerns regarding hazard associated with induced seismicity. In current hazard-mapping practice for building code applications, the contributions from induced seismicity are intentionally excluded (Petersen *et al.*, 2015). However, in regions of low-to-moderate natural seismicity such as Oklahoma, the hazard from induced earthquakes may exceed that from natural background seismicity, if a sequence is stimulated in close proximity to a site (Atkinson, Ghofrani, and Assatourians, 2015). Therefore, it is important to understand to what extent induced events contribute to the overall hazard.

Estimation of ground motions that can be produced by induced earthquakes is key to determining hazard
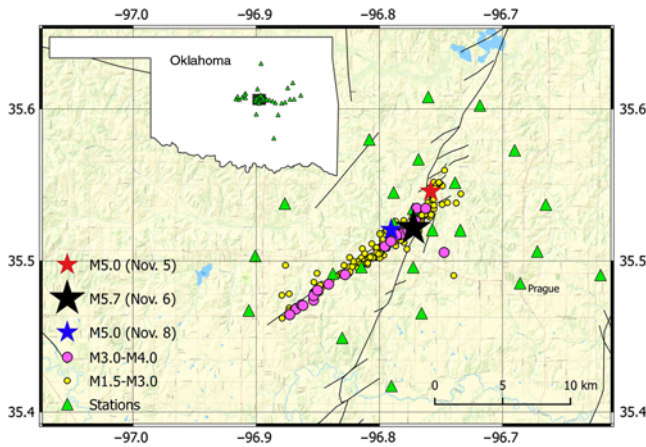
Figure 1. Epicenters of study events of $\mathbf{M} > 1.5$ from the 2011 Prague, Oklahoma, sequence, between November 2011 and December 2011, as determined by Sumy *et al.* (2014). Inset map shows location. Triangles are recording stations and lines show fault systems in the region (from Holland, 2015). The color version of this figure is available only in the electronic edition.

contributions from induced seismicity, but is a challenging problem due to the paucity of applicable ground-motion data. Recently, Yenier and Atkinson (2015b; hereafter, YA15) developed a generic ground-motion prediction equation (GMPE) that can be adjusted for use in any region by modifying a few key model parameters. As an example implementation, YA15 calibrated the generic model to develop a GMPE for central and eastern North America (CENA) that captures the source and attenuation attributes of ground motions observed in the region. In this study, we aim to tune the CENA model to obtain a GMPE that is calibrated for induced earthquakes in Oklahoma, and which is applicable over a wide range of magnitude and distance. To this end, we investigate the region-specific source and attenuation attributes of induced events in Oklahoma, using ground motions obtained from the 2011 Prague earthquake sequence.

In this article, we consider all Prague events to be part of an induced seismic sequence. One could argue that only the first event was directly induced by wastewater injection, and that the subsequent events were a combination of triggered events and aftershocks that were not directly caused by wastewater injection. However, from a hazard viewpoint this distinction is not particularly relevant or helpful, as our interest lies in what levels of ground motion might be caused by such events. Moreover, it has been noted that there appears to be no difference between natural and induced earthquakes in terms of the source parameters that control ground motion, for the same magnitude and focal depth (Yenier and Atkinson, 2015b); thus it is not necessary from a ground-motion perspective to make such a distinction. We acknowledge an implicit assumption that other induced sequences in Oklahoma will have similar ground-motion characteristics to those of the Prague sequence. This will be tested in future studies with additional ground-motion datasets.

Regionally Adjustable Generic GMPE

Yenier and Atkinson (2015b) developed a generic GMPE suitable for use in a variety of applications, using a simulation-based model whose parameters were calibrated using the rich California ground-motion database (Yenier and Atkinson, 2015a); the model calibration to the California database ensures realistic magnitude scaling and near-distance saturation effects for earthquakes as large as moment magnitude $\mathbf{M}$ 8. They parameterized the generic model so as to separate the influence of source and attenuation parameters on ground-motion amplitudes in the functional form. This provides a plug-and-play model that is adjustable for use in any region by modifying a few key model parameters. The utility of the generic GMPE is that one can easily produce a regional prediction equation by entering the associated source and attenuation parameters into the generic GMPE, without needing to perform multiple simulations and calculating model coefficients. This is an efficient and robust way to develop stable GMPEs that are calibrated for regional parameters, but have behavior that is tied to well-known seismological models.

One can also use the generic GMPE to compute the regional values of source and attenuation parameters from ground-motion data. The underlying model assumption is that the magnitude scaling behavior and close-distance saturation effects of the generic GMPE are transferable between regions. No such assumption is made regarding the overall amplitude level and attenuation; these properties can be adjusted for region-specific applications by modifying the associated parameters (discussed later). The generic GMPE facilitates the extrapolation of an empirically adjusted model in a seismologically informed way, enabling reliable ground-motion predictions for magnitudes and distances where observations are sparse.

The functional form of the generic GMPE is given as

$$\ln Y = F_E + F_Z + F_\gamma + F_S + C, \qquad (1)$$

in which $\ln Y$ is the natural logarithm of a ground-motion intensity measure: peak ground acceleration (PGA, in units of g), peak ground velocity (PGV, in units of cm/s), and 5% damped pseudospectral acceleration (PSA, in units of g). F_E, F_Z, F_γ, and F_S represent functions for earthquake source, geometrical spreading, anelastic attenuation, and site effects, respectively. The C term is an empirical calibration factor that accounts for residual effects that are different from or missing in simulations, resulting in an overall discrepancy in amplitude level between simulations and observations (i.e., a constant offset). The source function (F_E) describes the decoupled effects of magnitude and stress on ground-motion amplitudes for magnitudes $\mathbf{M}$ 3–8:

$$F_E = F_M + F_{\Delta\sigma}, \qquad (2)$$

in which F_M represents the magnitude effect on ground-motion amplitudes that would be observed at the source, if there were no saturation effects. It was determined from

Table 1
Model Coefficients for the Magnitude Scaling (F_M) and Geometrical Spreading (F_Z) Functions

T (s)	$\mathbf{M_h}$	e_0	e_1	e_2	e_3	b_3	b_4
0.010	5.85	2.227	6.874×10^{-1}	-1.363×10^{-1}	7.643×10^{-1}	-6.209×10^{-1}	6.057×10^{-2}
0.013	5.90	2.281	6.855×10^{-1}	-1.290×10^{-1}	7.617×10^{-1}	-6.259×10^{-1}	6.129×10^{-2}
0.016	5.85	2.272	6.971×10^{-1}	-1.232×10^{-1}	7.594×10^{-1}	-6.308×10^{-1}	6.191×10^{-2}
0.020	5.90	2.378	6.999×10^{-1}	-1.066×10^{-1}	7.488×10^{-1}	-6.377×10^{-1}	6.251×10^{-2}
0.025	6.00	2.564	6.840×10^{-1}	-9.416×10^{-2}	7.413×10^{-1}	-6.311×10^{-1}	6.097×10^{-2}
0.030	6.15	2.806	6.607×10^{-1}	-9.087×10^{-2}	7.389×10^{-1}	-6.028×10^{-1}	5.641×10^{-2}
0.040	5.75	2.731	7.034×10^{-1}	-1.086×10^{-1}	7.383×10^{-1}	-5.484×10^{-1}	4.820×10^{-2}
0.050	5.35	2.559	7.193×10^{-1}	-1.636×10^{-1}	7.545×10^{-1}	-5.096×10^{-1}	4.279×10^{-2}
0.065	5.75	2.997	6.842×10^{-1}	-1.547×10^{-1}	7.553×10^{-1}	-4.665×10^{-1}	3.640×10^{-2}
0.080	5.20	2.576	7.651×10^{-1}	-2.434×10^{-1}	7.865×10^{-1}	-4.210×10^{-1}	3.071×10^{-2}
0.100	5.45	2.777	7.118×10^{-1}	-2.619×10^{-1}	7.941×10^{-1}	-3.774×10^{-1}	2.472×10^{-2}
0.130	5.35	2.641	7.346×10^{-1}	-3.321×10^{-1}	8.116×10^{-1}	-3.551×10^{-1}	2.224×10^{-2}
0.160	5.25	2.466	8.088×10^{-1}	-3.871×10^{-1}	8.407×10^{-1}	-3.265×10^{-1}	1.918×10^{-2}
0.200	5.45	2.549	8.194×10^{-1}	-3.860×10^{-1}	8.426×10^{-1}	-2.868×10^{-1}	1.376×10^{-2}
0.250	5.60	2.517	8.671×10^{-1}	-3.775×10^{-1}	8.785×10^{-1}	-2.429×10^{-1}	9.209×10^{-3}
0.300	5.85	2.635	8.471×10^{-1}	-3.631×10^{-1}	8.763×10^{-1}	-2.117×10^{-1}	5.164×10^{-3}
0.400	6.15	2.674	8.501×10^{-1}	-3.469×10^{-1}	8.966×10^{-1}	-1.927×10^{-1}	4.847×10^{-3}
0.500	6.25	2.544	8.856×10^{-1}	-3.486×10^{-1}	9.182×10^{-1}	-2.079×10^{-1}	8.540×10^{-3}
0.650	6.60	2.617	8.758×10^{-1}	-3.160×10^{-1}	9.251×10^{-1}	-2.277×10^{-1}	1.371×10^{-2}
0.800	6.85	2.664	9.053×10^{-1}	-2.888×10^{-1}	8.944×10^{-1}	-2.523×10^{-1}	1.906×10^{-2}
1.000	6.45	1.986	1.340	-2.456×10^{-1}	9.829×10^{-1}	-2.974×10^{-1}	2.765×10^{-2}
1.300	6.75	2.011	1.386	-2.057×10^{-1}	1.000	-3.503×10^{-1}	3.777×10^{-2}
1.600	6.75	1.753	1.564	-1.678×10^{-1}	1.054	-3.849×10^{-1}	4.430×10^{-2}
2.000	6.65	1.251	1.748	-1.316×10^{-1}	1.192	-4.353×10^{-1}	5.361×10^{-2}
PGA	5.85	2.216	6.859×10^{-1}	-1.392×10^{-1}	7.656×10^{-1}	-6.187×10^{-1}	6.029×10^{-2}
PGV	5.90	5.960	1.030	-1.651×10^{-1}	1.079	-5.785×10^{-1}	5.737×10^{-2}

PGA, peak ground acceleration; PGV, peak ground velocity.

simulations for a reference stress ($\Delta\sigma = 100$ bar), near-surface attenuation parameter ($\kappa_0 = 0.025$ s), and site condition (National Earthquake Hazards Reduction Program [NEHRP], 2000, B/C site condition). $F_{\Delta\sigma}$ represents the stress adjustment factor that is applied when the stress parameter ($\Delta\sigma$) is different than its reference value (100 bars).

The F_M term uses a hinged-quadratic function that is adopted from the empirical Next Generation Attenuation-West2 Project (NGA-West2) GMPE of Boore *et al.* (2014):

$$F_M = \begin{cases} e_0 + e_1(\mathbf{M} - \mathbf{M}_h) + e_2(\mathbf{M} - \mathbf{M}_h)^2 & \mathbf{M} \le \mathbf{M}_h \\ e_0 + e_3(\mathbf{M} - \mathbf{M}_h) & \mathbf{M} > \mathbf{M}_h \end{cases}, \quad (3)$$

in which the hinge magnitude $\mathbf{M}_h$ and model coefficients e_0 to e_3 are period dependent. The coefficients of F_M function, as determined from simulations by YA15, are given in Table 1. The stress adjustment term is defined as

$$F_{\Delta\sigma} = e_{\Delta\sigma} \ln(\Delta\sigma/100), \quad (4)$$

in which $e_{\Delta\sigma}$ is the rate of ground-motion scaling with $\Delta\sigma$. Equation (4) describes the relationship between stress parameter and response spectral amplitudes, facilitating determination of its value from observed PSA data (e.g., Atkinson, Hassani, *et al.*, 2015; Yenier and Atkinson, 2015b). The stress scaling term ($e_{\Delta\sigma}$), as determined from the simulations, is given as a function of magnitude and period, and differs

depending on whether stress is up- or down-scaled relative to its reference value (100 bars). YA15 found that $e_{\Delta\sigma}$ is best described by a high-order polynomial:

$$e_{\Delta\sigma} = \begin{cases} s_0 + s_1\mathbf{M} + s_2\mathbf{M}^2 + s_3\mathbf{M}^3 + s_4\mathbf{M}^4 & \Delta\sigma \le 100 \text{ bar} \\ s_5 + s_6\mathbf{M} + s_7\mathbf{M}^2 + s_8\mathbf{M}^3 + s_9\mathbf{M}^4 & \Delta\sigma > 100 \text{ bar} \end{cases},$$
$$(5)$$

in which s_0 to s_9 are period-dependent model coefficients, reproduced from YA15 in Table 2. Figure 2 shows the variation of response spectra with magnitude and stress based on the source function (F_E). Ground motions are primarily controlled by $\mathbf{M}$ at periods longer than the corner period ($T_c = 1/f_c$, in which f_c is the corner frequency of the theoretical Brune, 1970 model), whereas $\Delta\sigma$ has limited effect on spectral amplitudes at periods $T > T_c$. The effect of the stress parameter increases with increasing magnitude and decreasing period.

In Figure 2, the magnitude scaling of ground motions weakens with increasing magnitude at close distances, because observed ground motions from large earthquakes ($\mathbf{M} > 6$) are controlled by the seismic radiation from only a portion of the fault rupture (Rogers and Perkins, 1996; Yenier and Atkinson, 2014). This results in near-distance saturation of ground-motion amplitudes with increasing magnitude. YA15 modeled these saturation effects using the equivalent point-source approach (Boore, 2009; Yenier

Table 2
Model Coefficients for the Stress Adjustment Factor ($F_{\Delta\sigma}$)

| T (s)	s_0	s_1	s_2	s_3	s_4	s_5	s_6	s_7	s_8	s_9
0.010	-2.048	1.881	-4.901×10^{-1}	5.668×10^{-2}	-2.433×10^{-3}	-1.437	1.242	-2.892×10^{-1}	3.088×10^{-2}	-1.252×10^{-3}
0.013	-1.922	1.802	-4.713×10^{-1}	5.471×10^{-2}	-2.357×10^{-3}	-1.348	1.195	-2.799×10^{-1}	3.006×10^{-2}	-1.225×10^{-3}
0.016	-1.711	1.663	-4.365×10^{-1}	5.087×10^{-2}	-2.199×10^{-3}	-1.079	1.041	-2.466×10^{-1}	2.690×10^{-2}	-1.114×10^{-3}
0.020	-1.160	1.274	-3.344×10^{-1}	3.911×10^{-2}	-1.700×10^{-3}	-1.272	1.254	-3.171×10^{-1}	3.624×10^{-2}	-1.550×10^{-3}
0.025	-1.535	1.595	-4.293×10^{-1}	5.103×10^{-2}	-2.242×10^{-3}	-1.454	1.366	-3.372×10^{-1}	3.727×10^{-2}	-1.537×10^{-3}
0.030	-1.056	1.205	-3.132×10^{-1}	3.615×10^{-2}	-1.550×10^{-3}	-2.243	1.981	-5.086×10^{-1}	5.782×10^{-2}	-2.439×10^{-3}
0.040	-8.571×10^{-1}	1.044	-2.677×10^{-1}	3.082×10^{-2}	-1.328×10^{-3}	-3.310	2.663	-6.683×10^{-1}	7.415×10^{-2}	-3.056×10^{-3}
0.050	-9.628×10^{-1}	9.826×10^{-1}	-2.156×10^{-1}	2.080×10^{-2}	-7.423×10^{-4}	-4.228	3.293	-8.316×10^{-1}	9.303×10^{-2}	-3.873×10^{-3}
0.065	-2.225	1.948	-4.900×10^{-1}	5.486×10^{-2}	-2.293×10^{-3}	-3.960	2.871	-6.675×10^{-1}	6.883×10^{-2}	-2.650×10^{-3}
0.080	-3.685	2.962	-7.510×10^{-1}	8.421×10^{-2}	-3.509×10^{-3}	-3.139	2.177	-4.674×10^{-1}	4.466×10^{-2}	-1.598×10^{-3}
0.100	-4.051	3.100	-7.625×10^{-1}	8.328×10^{-2}	-3.393×10^{-3}	-2.452	1.569	-2.890×10^{-1}	2.300×10^{-2}	-6.573×10^{-4}
0.130	-4.174	3.092	-7.438×10^{-1}	7.982×10^{-2}	-3.205×10^{-3}	-1.384	6.264×10^{-1}	-1.161×10^{-2}	-1.092×10^{-2}	8.284×10^{-4}
0.160	-3.965	2.820	-6.499×10^{-1}	6.720×10^{-2}	-2.614×10^{-3}	-1.997×10^{-1}	-3.370×10^{-1}	2.570×10^{-1}	-4.252×10^{-2}	2.176×10^{-3}
0.200	-2.707	1.729	-3.302×10^{-1}	2.816×10^{-2}	-9.064×10^{-4}	8.197×10^{-1}	-1.083	4.395×10^{-1}	-6.105×10^{-2}	2.846×10^{-3}
0.250	-1.767	9.826×10^{-1}	-1.314×10^{-1}	5.998×10^{-3}	-1.162×10^{-5}	1.780	-1.767	6.066×10^{-1}	-7.834×10^{-2}	3.498×10^{-3}
0.300	-3.182×10^{-1}	-1.386×10^{-1}	1.704×10^{-1}	-2.850×10^{-2}	1.421×10^{-3}	2.245	-2.003	6.326×10^{-1}	-7.699×10^{-2}	3.268×10^{-3}
0.400	2.018	-1.857	6.117×10^{-1}	-7.674×10^{-2}	3.341×10^{-3}	2.422	-1.938	5.558×10^{-1}	-6.174×10^{-2}	2.390×10^{-3}
0.500	3.956	-3.288	9.885×10^{-1}	-1.196×10^{-1}	5.142×10^{-3}	8.555×10^{-1}	-4.528×10^{-1}	6.459×10^{-2}	5.220×10^{-3}	-8.299×10^{-4}
0.650	3.645	-2.822	7.932×10^{-1}	-8.926×10^{-2}	3.555×10^{-3}	-6.671×10^{-1}	9.277×10^{-1}	-3.708×10^{-1}	6.183×10^{-2}	-3.430×10^{-3}
0.800	2.404	-1.652	4.088×10^{-1}	-3.710×10^{-2}	1.051×10^{-3}	-2.124	2.152	-7.301×10^{-1}	1.053×10^{-1}	-5.287×10^{-3}
1.000	1.066	-4.552×10^{-1}	3.739×10^{-2}	1.033×10^{-2}	-1.084×10^{-3}	-4.473	4.051	-1.274	1.710×10^{-1}	-8.137×10^{-3}
1.300	-2.508	2.523	-8.446×10^{-1}	1.205×10^{-1}	-6.024×10^{-3}	-5.494	4.766	-1.439	1.849×10^{-1}	-8.458×10^{-3}
1.600	-5.264	4.738	-1.476	1.963×10^{-1}	-9.284×10^{-3}	-5.880	4.978	-1.465	1.832×10^{-1}	-8.156×10^{-3}
2.000	-6.642	5.767	-1.742	2.241×10^{-1}	-1.028×10^{-2}	-6.010	4.985	-1.433	1.748×10^{-1}	-7.587×10^{-3}
PGA	-2.132	1.937	-5.040×10^{-1}	5.824×10^{-2}	-2.498×10^{-3}	-1.444	1.235	-2.851×10^{-1}	3.021×10^{-2}	-1.217×10^{-3}
PGV	-2.246	1.951	-5.181×10^{-1}	6.139×10^{-2}	-2.725×10^{-3}	-1.758	1.379	-3.256×10^{-1}	3.500×10^{-2}	-1.425×10^{-3}
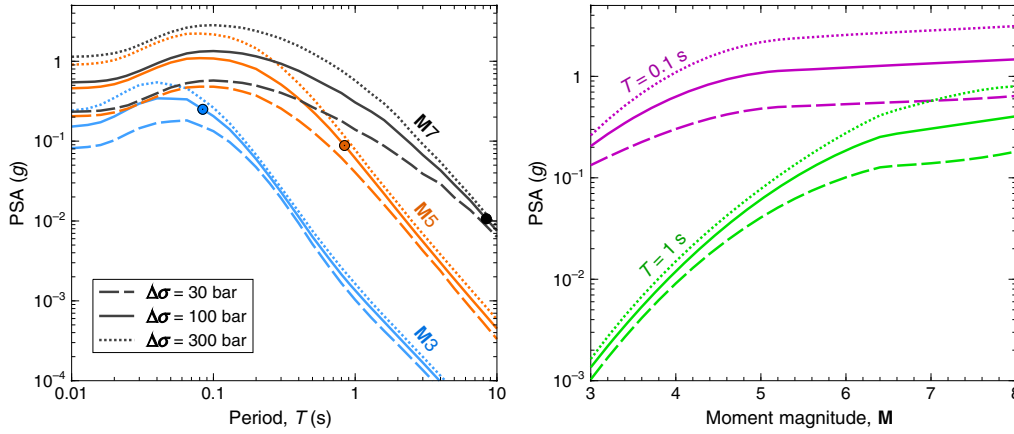
Figure 2. Pseudospectral acceleration (PSA) given by the generic ground-motion prediction equation (GMPE). Ground motions are shown for rupture distance $D_{\text{rup}} = 1$ km, for alternative $\Delta\sigma$ values. At left, the circles represent corner periods (T_c) for the reference stress (100 bars). The color version of this figure is available only in the electronic edition.

and Atkinson, 2014), in which the geometrical spreading (F_Z) is defined as

$$F_Z = \ln(Z) + (b_3 + b_4\mathbf{M})\ln(R/R_{\text{ref}}). \quad (6)$$

R represents the effective distance metric:

$$R = \sqrt{D_{\text{rup}}^2 + h^2}, \quad (7)$$

in which D_{rup} is the rupture distance (measured from the closest point on the rupture surface to the site). For small events, the closest distance can be assumed equivalent to the hypocentral distance (i.e., $D_{\text{rup}} \approx D_{\text{hyp}}$). h is a pseudo-depth term that accounts for saturation effects:

$$h = 10^{-0.405 + 0.235\mathbf{M}}. \quad (8)$$

In equation (6), Z represents the geometrical attenuation of Fourier amplitudes, and $(b_3 + b_4\mathbf{M})\ln(R/R_{\text{ref}})$ accounts for the change in the apparent attenuation that occurs when ground motions are modeled in the response spectral domain rather than the Fourier domain. The coefficients b_3 and b_4 are period dependent, as adopted from YA15 in Table 1. The reference distance is defined as $R_{\text{ref}} = \sqrt{1 + h^2}$.

Z is a hinged bilinear model that provides for a transition from direct-wave spreading to surface-wave spreading of reflected and refracted waves:

$$Z = \begin{cases} R^{b_1} & R \leq R_t, \\ R_t^{b_1}(R/R_t)^{b_2} & R > R_t, \end{cases} \quad (9)$$

in which R_t represents the transition distance, and b_1 and b_2 are the geometrical attenuation rates of Fourier amplitudes at $R \leq R_t$ and $R > R_t$, respectively. YA15 defined the geometrical spreading parameters at their generic values suggested for western and eastern North America (Atkinson and Boore, 2014; Yenier and Atkinson, 2015a): $b_1 = -1.3$, $b_2 = -0.5$, and $R_t = 50$ km. Figure 3 shows the decay of ground

motions due to geometrical spreading effects as given by equation (6).

The F_Z function effectively separates the geometrical spreading of Fourier amplitudes (Z) from the change in apparent attenuation that occurs when ground motions are convolved by the response spectra transfer function. This separation is a key element of the generic GMPE, resulting in a plug-and-play feature in which a new GMPE can be defined for a specified attenuation rate in the Fourier domain, without the need to reperform simulations.

The anelastic attenuation function (F_γ) is given as

$$F_\gamma = \gamma D_{\text{rup}}, \quad (10)$$

in which γ is a period-dependent anelastic attenuation coefficient that is empirically determined from regional ground-motion data.

The generic GMPE is defined relative to the reference NEHRP B/C boundary site condition (travel-time weighted average shear-wave velocity over the top 30 m, $V_{S30} = 760$ m/s). Site effects at different site conditions are modeled by the F_S term, which can be either determined from empirical regression or adopted from a standard empirical site-response model.

The generic GMPE distills the effects of key seismological parameters on ground-motion amplitudes. It can be adjusted to a specific region by modifying the source and attenuation parameters, and determining an overall empirical calibration factor (C) that represents residual effects that are missing or different in simulations compared to ground-motion amplitude observations. The magnitude (F_M) and saturation (h) effects in the generic model, as determined from data-rich regions, are assumed to be transferable to other regions. However, the stress parameter, geometrical spreading, and anelastic attenuation may show regional variations. The generic GMPE can be readily adjusted for regional source and attenuation effects by plugging the regional values of $\Delta\sigma$, Z, and γ into equations (4), (6), and
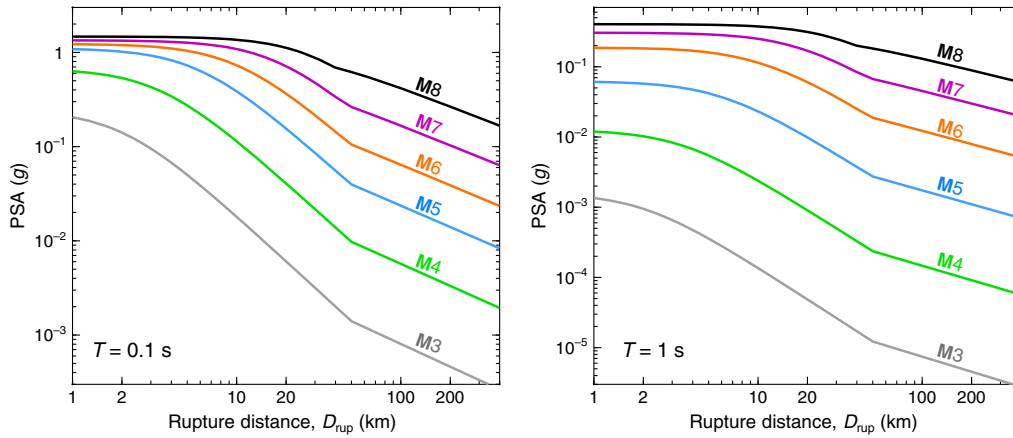
Figure 3. Ground-motion attenuation with distance, based on generic geometrical spreading function (F_Z). No anelastic attenuation is considered in this example. The color version of this figure is available only in the electronic edition.

(10), respectively. Although the saturation effects are fixed in the generic GMPE and are assumed to be transferable between regions, equation (6) allows for its modification if there is compelling evidence supporting such a change. The calibration factor C is calculated through the analysis of residuals between observed motions and the GMPE obtained after other regional adjustments.

In an example application, YA15 adjusted the generic GMPE to develop a predictive model for CENA using the NGA-East ground-motion dataset compiled from earthquakes in the central and eastern United States and southeastern Canada (excluding the Gulf Coast region). This database comprised mostly natural earthquakes, but included nine induced events, eight of which were from Oklahoma and Arkansas. YA15 derived a magnitude- and depth-dependent stress model ($\Delta\sigma_{CENA}$), based on matching observed spectral shapes of CENA events. They adopted the generic Z model (equation 9: $b_1 = -1.3$, $b_2 = -0.5$, and $R_t = 50$ km) without modification, based on the findings of attenuation studies in the region (Babaie Mahani and Atkinson, 2012; Atkinson and Boore, 2014), and determined regional anelastic attenuation (γ_{CENA}) and calibration factor (C_{CENA}) from the empirical data. The CENA GMPE was obtained by plugging the derived stress and attenuation models as well as the regional calibration factor into the generic model:

$$\ln Y_{CENA} = F_M + F_{\Delta\sigma CENA} + F_Z$$
$$+ \gamma_{CENA} D_{rup} + F_S + C_{CENA}. \quad (11)$$

$F_{\Delta\sigma CENA}$ represents the stress adjustment term (equation 4) evaluated for the CENA stress parameter model ($\Delta\sigma_{CENA}$):

$$\ln \Delta\sigma_{CENA} = 5.704 + \min[0, 0.29(d - 10)]$$
$$+ \min[0, 0.229(\mathbf{M} - 5)], \quad (12)$$

in which d is the focal depth in kilometers. The calibration factor (C_{CENA}) is given as the summation of event and path calibrations, determined from observed ground motions in CENA (see Yenier and Atkinson, 2015b, for further details).
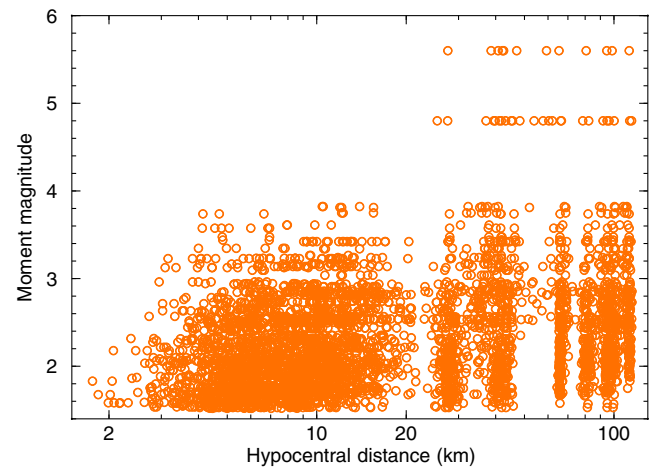
Figure 4. Magnitude–distance distribution of the ground-motion dataset obtained from the 2011 Prague sequence, for $\mathbf{M} > 1.5$ events. The color version of this figure is available only in the electronic edition.

Oklahoma Ground-Motion Dataset

In this study, we refine the regional parameters of the CENA GMPE as needed to better characterize ground motions of induced earthquakes in Oklahoma, considering the ground motions recorded during the 2011 Prague earthquake sequence. The ground-motion dataset consists of 4216 three-component recordings obtained from 291 earthquakes ($\mathbf{M} > 1.5$) detected between November 2011 and December 2011. Figure 4 shows the magnitude–distance distribution of the database. The record processing to obtain the PSA database used in the study is described by Sumy *et al.* (2014). In brief, they supplemented permanent array data with records obtained on a dense local array deployed in November 2011. Event locations obtained from the local array are considered accurate to within about 100 m. All records were uniformly processed to correct for instrument response. The signal window for the response spectra begins with the P arrival and is

Table 3
Seismological Parameters of the 2011 Prague, Oklahoma, Events (M ≥ 2.7) for Which Stress Parameter Is Calculated

Event ID*	Date (yyyy/mm/dd)	Time (hh:mm:ss)	Latitude (°)	Longitude (°)	Depth (km)	M	$\Delta\sigma$ (bar)
1	**2011/11/05**	**07:12:45**	**35.5456**	**−96.7583**	**3.65**	**5.00**	**166.0**
2	2011/11/05	09:12:11	35.5200	−96.7769	3.68	3.42	22.9
3	**2011/11/06**	**03:53:10**	**35.5215**	**−96.7725**	**2.96**	**5.70**	**131.8**
4	2011/11/06	04:03:41	35.5179	−96.7816	4.38	3.48	302.0
5	2011/11/06	04:31:50	35.5178	−96.7808	4.42	3.44	316.2
6	2011/11/06	04:53:59	35.5343	−96.7625	6.01	3.10	87.1
7	2011/11/06	06:31:11	35.4709	−96.8632	5.82	3.75	43.7
8	2011/11/06	07:32:41	35.4770	−96.8535	5.64	3.17	6.9
9	2011/11/06	08:14:13	35.5214	−96.7816	5.87	2.92	104.7
10	2011/11/06	09:22:04	35.4794	−96.8515	5.12	3.34	6.6
11	2011/11/06	09:39:57	35.4681	−96.8678	4.35	3.81	4.2
12	2011/11/06	10:52:35	35.5170	−96.7843	3.52	3.74	7.6
13	2011/11/06	11:03:52	35.4846	−96.8412	4.70	3.26	39.8
14	2011/11/06	11:16:20	35.4824	−96.8468	4.35	2.88	25.1
15	2011/11/06	13:37:36	35.4662	−96.8738	4.70	2.86	63.1
16	2011/11/06	15:07:06	35.4740	−96.8535	3.51	3.82	4.2
17	2011/11/06	17:52:35	35.4909	−96.8279	3.84	3.61	3.3
18	2011/11/06	18:26:57	35.4644	−96.8728	5.99	3.24	3.2
19	2011/11/06	19:31:38	35.4979	−96.8139	3.24	2.74	21.9
20	2011/11/07	00:03:51	35.4975	−96.8097	3.34	2.85	20.9
21	2011/11/07	01:17:13	35.5169	−96.7861	6.20	3.23	47.9
22	2011/11/07	01:26:31	35.5096	−96.7956	3.59	3.35	79.4
23	2011/11/07	08:00:58	35.4646	−96.8741	5.65	2.74	28.8
24	2011/11/07	08:12:35	35.5096	−96.7962	3.09	2.76	22.9
25	2011/11/07	08:19:54	35.5184	−96.7772	2.78	2.71	26.3
26	2011/11/07	13:50:20	35.4705	−96.8621	5.74	3.04	22.9
27	2011/11/07	16:00:23	35.4633	−96.8737	6.38	2.77	30.2
28	2011/11/07	17:09:51	35.5032	−96.8004	3.33	2.94	9.1
29	**2011/11/08**	**02:46:57**	**35.5203**	**−96.7905**	**4.00**	**5.00**	**263.0**
30	2011/11/08	03:05:07	35.5201	−96.7949	2.85	2.96	11.5
31	2011/11/08	19:05:18	35.5174	−96.7834	4.02	3.58	398.1
32	2011/11/09	10:11:40	35.5183	−96.7951	3.51	2.78	120.2
33	2011/11/09	12:08:36	35.5258	−96.7704	2.94	3.13	28.8
34	2011/11/10	08:36:38	35.4806	−96.8503	3.68	3.17	5.0
35	2011/11/11	19:19:16	35.5334	−96.7572	5.08	2.94	15.8
36	2011/11/12	01:18:42	35.5439	−96.7339	4.69	2.84	19.1
37	2011/11/12	01:41:03	35.5328	−96.7606	6.04	2.81	87.1
38	2011/11/14	05:31:42	35.5129	−96.7907	2.88	3.23	5.8
39	2011/11/16	17:10:52	35.5015	−96.8099	7.69	2.91	15.8
40	2011/11/18	07:41:08	35.5348	−96.7618	9.49	2.81	83.2
41	2011/11/20	05:54:02	35.5505	−96.7504	4.36	2.73	72.4
42	2011/11/21	21:46:09	35.5001	−96.8167	5.68	2.85	120.2
43	2011/11/24	21:11:04	35.5344	−96.7697	9.03	3.42	125.9
44	2011/11/25	21:24:29	35.5056	−96.7475	6.05	3.14	39.8
45	2011/11/29	09:22:33	35.5327	−96.7674	6.26	2.73	36.3
46	2011/12/03	04:42:12	35.5270	−96.7702	9.86	2.82	125.9

*The three M ≥ 5.0 mainshocks are indicated in bold.

at least 40 s in length, depending on the distance of the record. The mean and trends are removed and a taper is applied. Records are retained only if the signal-to-noise ratio exceeds two over at least an 8 Hz bandwidth. High-pass filtering is performed to remove long-period noise, and spectral information is retained only for frequencies greater than 1.5 times the high-pass frequency. Response spectra (5% damped PSA) are calculated from instrument-corrected accelerograms. The horizontal-component PSA is taken as the geometric mean of the two components.

The moment magnitudes for the study events were assigned as follows. For the three M ≥ 5.0 Prague mainshocks, we use the Global CMT catalog values (Table 3). For other events (M < 4), we estimate M based on the observed vertical-component response spectral ordinates at periods $T = 1$ s and/or $T = 0.3$ s, following Atkinson, Greig, and Yenier (2014) and Novakovic and Atkinson (2015), assuming the CENA attenuation model (this model attenuation matches the Z model given by equation 9); for the M estimates we use only the PSA values with hypocentral distances $D_{hyp} < 50$ km, to reduce
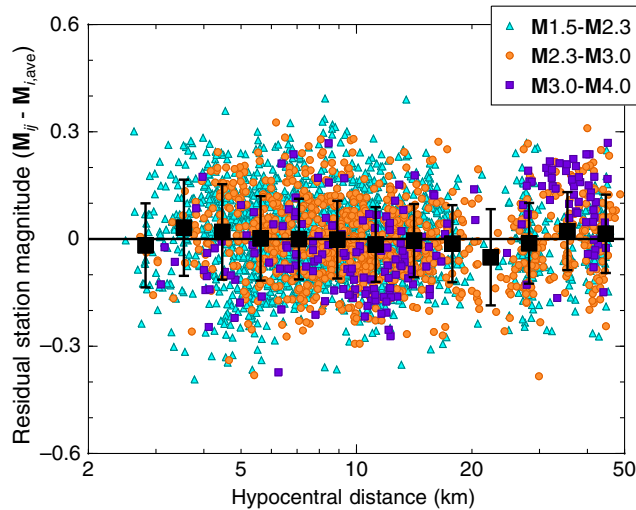
Figure 5. Magnitude residuals as a function of distance. Residuals coded based on event-magnitude bins. Large squares show mean residual calculated for distance bins of 0.1 log-unit intervals and error bars indicate one standard deviation about the mean. The color version of this figure is available only in the electronic edition.

noise effects. We examine the behavior of the station residuals (the difference between the estimated $\mathbf{M}$ for event i at station j and the average $\mathbf{M}$ obtained from all stations of that event, $\mathbf{M}_{ij,\mathrm{res}} = \mathbf{M}_{ij} - \mathbf{M}_{i,\mathrm{ave}}$), to assess the compatibility of the assumed attenuation model. The ground-motion attenuation is primarily controlled by geometric spreading at close distances. On average, the magnitude residuals show no distance-dependent trends within 50 km, as shown in Figure 5. This suggests that the geometric spreading of ground motions in Oklahoma agrees with the generic Z model used in the magnitude determination. However, there is an exception for $\mathbf{M}$ 3–4 events, as seen in Figure 5. Residuals of $\mathbf{M}$ 3–4 events generally have negative values at distances between 8 and 15 km, yet they are positive from 25 to 50 km. This discrepancy appears to be specific to the aforementioned distance ranges. It might be due to the mapping of unresolved effects (e.g., site amplification, radiation pattern, and localized attenuation attributes) into the residuals. For $\mathbf{M}$ 3–4 events, residuals at close distances ($D_{\mathrm{hyp}} < 8$ km) are near zero. Overall, we conclude that the generic Z model is compatible with ground-motion attenuation in Oklahoma.

We compared the PSA-based $\mathbf{M}$ estimates with those reported by McNamara *et al.* (2015) and the U.S. Geological Survey National Earthquake Information Center (USGS NEIC). McNamara *et al.* (2015) determined regional moment tensors (RMTs) for well-recorded events in Oklahoma from 2009 to 2014. There are 34 events in our dataset for which McNamara *et al.* (2015) also computed $\mathbf{M}$, and eight events for which $\mathbf{M}$ was reported by the USGS NEIC. Figure 6 shows that there is reasonable agreement between magnitude estimates for $\mathbf{M} > 2.7$ events, with the agreement being better for the larger events reported by the NEIC. However, PSA-based magnitudes tend to have larger values than those obtained from RMT solutions for $\mathbf{M} < 2.7$ events. This may be due
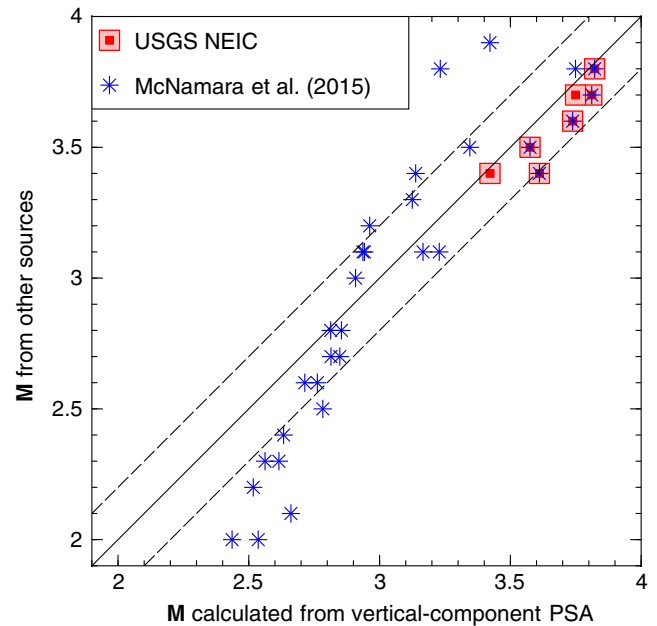
Figure 6. Comparison of moment magnitudes ($\mathbf{M}$) determined from response spectra and those reported by the U.S. Geological Survey National Earthquake Information Center (USGS NEIC) and McNamara *et al.* (2015). Solid line is 1:1 relation; dashed lines show ± 0.2 magnitude units about the solid line. The color version of this figure is available only in the electronic edition.

to oscillator response being driven by long-period noise for weak motions (Novakovic and Atkinson, 2015).

Calibration of Generic GMPE for Induced Earthquakes in Oklahoma

We calibrate the CENA GMPE using ground motions obtained from $\mathbf{M} \geq 2.7$ events of the Prague sequence, as listed in Table 3; this includes 949 recordings obtained from 46 events at 44 stations. We consider only those stations and events with at least five recordings to ensure that the determined source and site terms are sufficiently constrained with empirical data. We assume that the generic magnitude scaling (equation 3) is applicable to induced events in Oklahoma and adopt the generic bilinear Z model (equation 9, $b_1 = -1.3$, $b_2 = -0.5$, and $R_t = 50$ km) without modification, based on the observations made in Figure 5. We can rewrite equation (11) for ground motions from induced Oklahoma events as

$$\ln Y_{\mathrm{OK},ij} - (F_{M,i} + F_{Z,ij} + \gamma_{\mathrm{CENA}} D_{\mathrm{rup},ij} + C_{\mathrm{CENA}})$$
$$= E_i + F_{S,j}, \qquad (13)$$

in which $Y_{\mathrm{OK},ij}$ represents the ground-motion amplitude for event i and station j. $F_{M,i}$ and $F_{Z,ij}$ are the magnitude-scaling and geometric spreading functions evaluated for the known magnitude ($\mathbf{M}$) and distance ($D_{\mathrm{rup},ij}$). We assume that hypocentral distance is equivalent to the rupture distance (i.e., $D_{\mathrm{rup}} \approx D_{\mathrm{hyp}}$). We adopt the anelastic attenuation determined from the CENA dataset (i.e., $\gamma_{\mathrm{OK}} = \gamma_{\mathrm{CENA}}$) to ensure reliable ground-motion estimates at far distances (we check
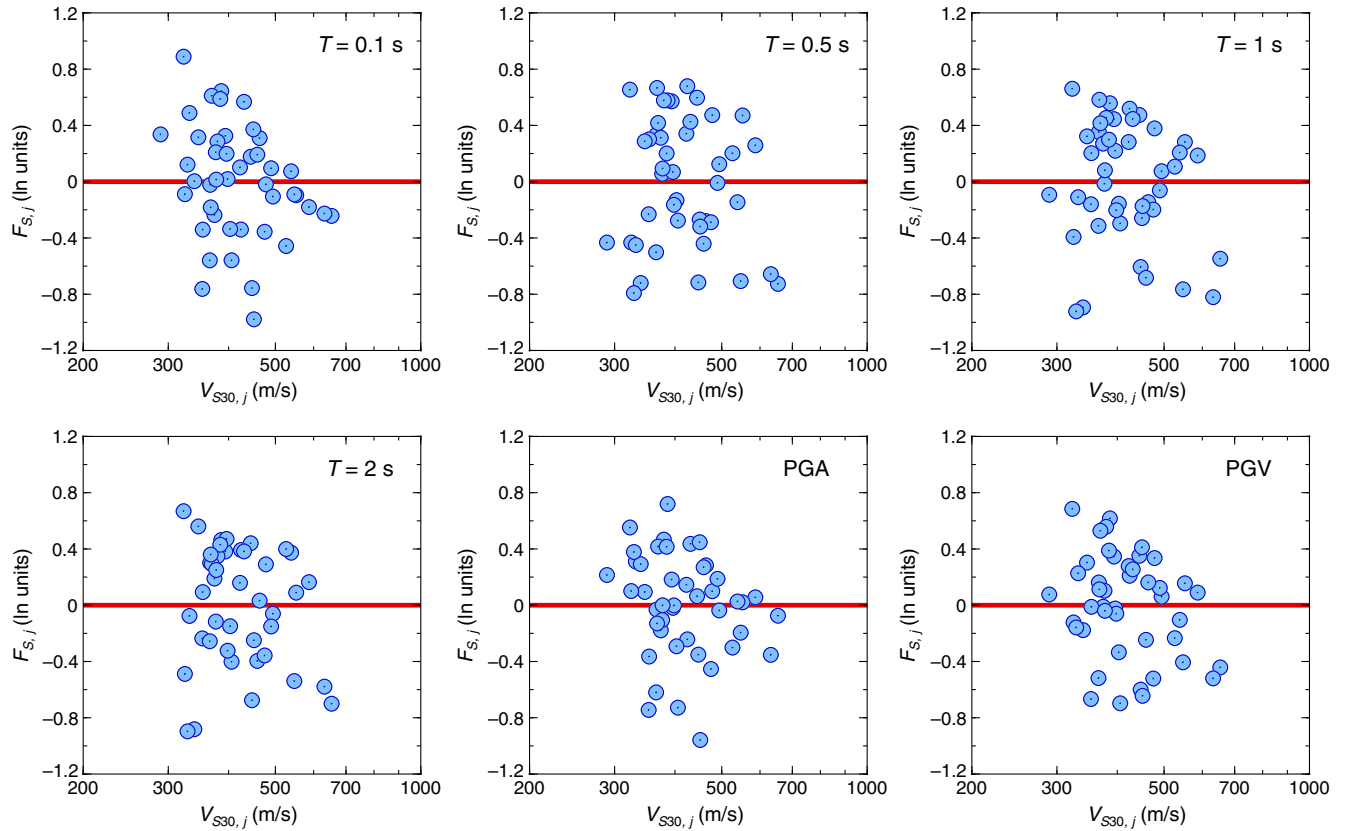
Figure 7. Comparison of site factors (F_S) with V_{S30} estimates based on topographic slope, for different spectral periods and peak motions. The solid line represents zero amplification (relative to average site response). Note that the horizontal axis is plotted in logarithmic scale. The color version of this figure is available only in the electronic edition.

this later by plotting residuals). In equation (13), E_i represents the event term that includes stress adjustment for event i ($F_{\Delta\sigma,i}$) and the Oklahoma calibration factor determined relative to the CENA model (ΔC_{OK}). $F_{S,j}$ represents the site effects for station j. We determine the event and site terms via empirical regressions, for average horizontal-component PGA, PGV, and 5% damped PSA at 24 log-spaced periods $T \leq 2$ s.

In ground-motion modeling, site effects are typically determined relative to a reference site condition to avoid trade-offs between source and site terms. YA15 defined the CENA GMPE relative to NEHRP B/C site boundary condition ($V_{S30} = 760$ m/s). In our dataset, site conditions are unknown for most of the stations. Based on the topographic slope proxy of Allen and Wald (2007, 2009), we infer that most stations are likely located on NEHRP C sites (360 m/s $< V_{S30} <$ 760 m/s) with an average $V_{S30} \approx 430$ m/s, with two stations that may be located on stiff sites ($V_{S30} > 600$ m/s). We do not attribute a high level of significance to the topography-based V_{S30} estimates; we simply use them as a rough guide to the average regional site conditions.

We determine site factors relative to the regional average by constraining the $F_{S,j}$ terms to attain zero when averaged over all stations. This allows the adjusted GMPE to be centered relative to the recorded ground motions, transferring the site-effect differences between the average site condition

(assumed to be C) and NEHRP B/C site into the regional calibration factor (discussed later). Figure 7 illustrates the site factors determined based on empirical regression of the observations to equation (13). F_S are in ln units and attain values between -1 and 1, showing no discernible trends with topography-based V_{S30} estimates.

The event term E_i represents the average adjustment required to match observed amplitudes from event i. Its value can be attributed to three main factors. One of them is the difference between the reference stress (100 bars) that is implicitly carried by the source function (F_M) and its actual value for event i. This discrepancy will be accounted for by the stress adjustment function ($F_{\Delta\sigma}$) in the calibrated GMPE. The second factor is the site-effect difference between the average site condition (NEHRP C) and the NEHRP B/C boundary condition, for which the F_M function was developed from simulations. The third factor is the overall residual effects that are different or missing in the CENA GMPE compared to observed motions in Oklahoma. The summation of the second and third factors can be represented by an Oklahoma calibration coefficient ΔC_{OK} to form a region-specific GMPE for induced earthquakes.

For a given event of known **M**, the stress parameter is determined from the observed spectral shape; this is equivalent to finding the corner frequency. Yenier and Atkinson (2015a)
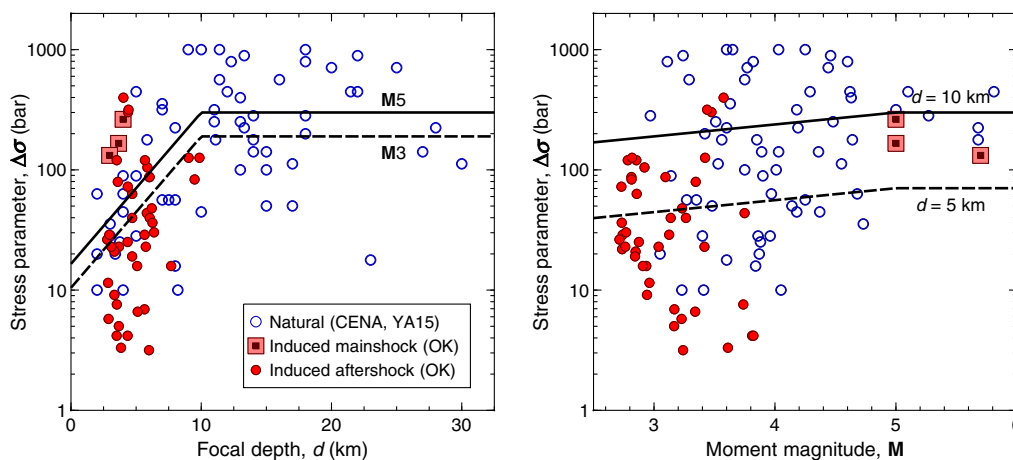
Figure 8. Best-fitting stress parameters ($\Delta\sigma$) determined for the induced Prague sequence as a function of focal depth and magnitude. Mainshocks and aftershocks are distinguished as indicated in the legend. Stress parameters determined from natural central and eastern North America (CENA) events by Yenier and Atkinson (2015b; hereafter, YA15) are also shown for comparison. Lines show the CENA $\Delta\sigma$ model of YA15, for different magnitudes and depths. The color version of this figure is available only in the electronic edition.

showed that the calculation of stress based on spectral shape breaks the trade-off between source and attenuation parameters. Following this technique, we determine $\Delta\sigma$ values for the induced Prague events by matching the shape of E_i and $F_{\Delta\sigma}$, over periods $T \leq 2$ s, where response spectra are generally well above the noise floor. The calculated stress parameters are listed in Table 3. These values implicitly assume a near-source shear-wave velocity (β) of 3.7 km/s, which is typical for the source depths of natural earthquakes. This assumption was made for consistency with the GMPE studies of Yenier and Atkinson (2015a,b) for natural events. However, for the shallow events of this sequence (depths ~3 km), near-source velocities may be in the range from 3.2 to 3.5 km/s (Herrmann *et al.*, 2015). Because the value of the stress parameter scales as $1/\beta^3$ (Boore, 2003), the equivalent values of stress parameter would be 20%–50% higher if this lower near-source velocity was taken into account.

Figure 8 shows the variation of $\Delta\sigma$ values for the study events, as a function of focal depth (d) and magnitude (**M**). The three largest events (**M** ≥ 5.0), which we consider to be mainshocks based on the findings of Keranen *et al.* (2013) and Sumy *et al.* (2014), have $\Delta\sigma$ values of 130–265 bars. This is consistent with typical stress values determined for natural events in CENA (d 5–10 km). On the contrary, the smaller events that follow each mainshock closely in both space and time, on the same fault plane, have much smaller stresses; we consider these smaller events as aftershocks to each of the respective mainshocks. The Prague aftershocks are characterized by a geometric-mean stress of $\Delta\sigma = 30$ bars, over all magnitudes. This value is lower than the mean stress observed for shallow natural events in CENA, by a factor of 1.5.

An interesting observation of Figure 8 concerns the variability of the stress parameter estimates for the induced sequence, in comparison to that for natural events in CENA. Prague events attain a standard deviation of 1.26 ln units (a factor of 3.5) in their stress parameters. This is slightly

larger than the variability of stress parameters determined from natural events in CENA (1.05 ln units; a factor of 2.9). However, an f-test of stress parameter variances suggest that this difference is not significant (p-value = 0.1). Spatiotemporal variations in source attributes of Prague aftershocks may contribute to the larger variance of stress parameters for induced events. This is investigated in the next section.

Spatiotemporal Evolution of Stress Parameter

On Figure 9, we show the location of the mainshock and aftershock events in map view. The **M** 5.7 and two **M** 5.0 mainshocks, and several of the aftershocks that are located near where the sequence was initiated, have relatively large $\Delta\sigma$ values in comparison to the rest of the events. We note that lower stress events extend down the southwest segment of the activated fault, possibly indicating an influence of differing fault properties on the stress parameter values. This pattern motivates us to examine the stress parameters as a function of time and distance from the associated mainshock. We identified aftershocks associated with each mainshock considering the time and location of each event. Specifically, events are distinguished as aftershocks if they occur within a few days following a mainshock (two days for the **M** 5.0 events, four days for the **M** 5.7 events), and appear to be along the same fault plane. For aftershocks that could potentially be associated with more than one mainshock by these criteria, the aftershock is associated with the nearest mainshock. Events that occurred after the conclusion of the identifiable aftershock sequences are considered to be following events, which are not specifically aftershocks of any of the three mainshock events. It is acknowledged that there is some subjectivity in this classification. As illustrated in Figure 10, the aftershocks for the largest event show a steeply decaying trend of stress parameter values with time, attaining values that are uniformly below 30 bars within one to two
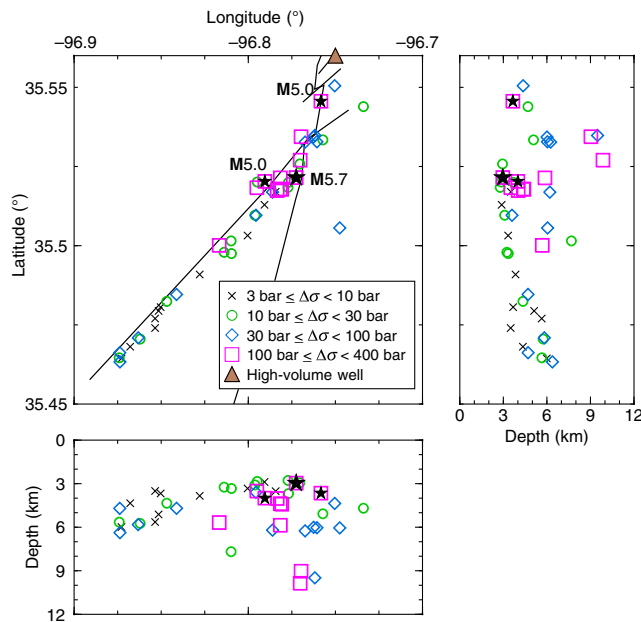
Figure 9. Spatial distribution of stress parameters (Δσ) for the induced Prague sequence. The locations of **M** ≥5.0 mainshocks are shown as stars. The Wilzetta fault system is shown by solid lines. The color version of this figure is available only in the electronic edition.

days. There is some suggestion of similar behavior for the two **M** 5.0 sequences, but they contain too few events to be definitive. Following the three decaying sequences, the events become more widely spaced in time, while the stress parameter values appear to recover. About a week after the third mainshock, the stress parameters have reset to average levels near 100 bars. We conclude that the CENA stress-parameter model of YA15 (equation 12) is appropriate for mainshock events in the Prague sequence, but that the aftershock events are characterized by lower stress parameter values.

We explore this intriguing temporal behavior within the short sequences of decaying stress that follow each mainshock in an expanded view, in which the distance from the mainshock is also shown, on Figure 11. The stress is clearly decaying in both distance and time from the associated mainshock for the largest event. It is noteworthy that this sequence extends to distances of 10 km and beyond from the associated hypocenter in a time span of only 1.5 days.

In considering the decay of the stress parameter with respect to time and space, it is interesting to explore the implications and potential causes. Presumably, the events in the sequence have been facilitated by high pore pressures traveling along the Wilzetta fault system, to distances of up to 18 km from a nearby high-volume disposal well shown in Figure 9 (Keranen *et al.*, 2013). Considering the temporal aspect of the stress parameter behavior, it has been suggested that permeability is enhanced by the mismatch of rough fault surfaces following fault slippage (Brown and Bruhn, 1998). This self-propping of the fault could allow elevated pore pressures to travel rapidly along it in the immediate aftermath
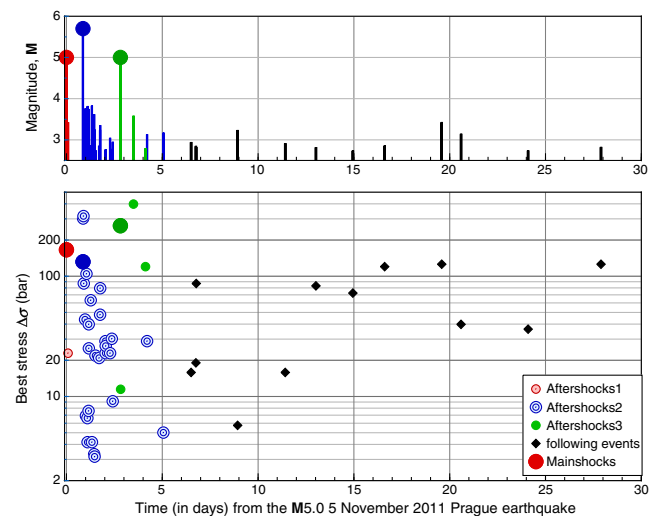

Figure 10. Temporal variation of (top) magnitude and (bottom) stress parameter for the 2011 Prague sequence. Different symbols distinguish aftershock sequences that appear to be associated with each mainshock. The color version of this figure is available only in the electronic edition.

of each mainshock rupture. These higher pore pressures would reduce effective stress and enable failure of asperities in a near-critical state. The higher-stress events may represent higher-strength asperities. The transient effects of mainshock slip may dissipate quickly, with stress readjustment subsequently occurring throughout the affected area.

Implications for Ground-Motion Prediction Equations

The stress parameter values obtained in this study, particularly the relatively high values for the mainshock events, may at first appear inconsistent with other studies. For example, other studies have concluded that induced earthquakes in Oklahoma have low-stress parameters (e.g., Hough, 2014; Sun and Hartzell, 2014; Sumy *et al.*, [unpublished manuscript, 2016; see Data and Resources]). However, the results do not appear discordant when considered more closely in the context of ground-motion amplitudes, which is the lens through which we are viewing the stress parameter values. For example, Sumy *et al.* (unpublished manuscript, 2016; see Data and Resources) looked at aftershock stress parameters for this sequence using a very different analysis model. The overall finding of low-stress parameters for the aftershocks, and a tendency for high-stress events to cluster near the mainshock initiation locations, are consistent in the two studies. However, Sumy *et al.* (unpublished manuscript, 2016; see Data and Resources) obtain systematically lower absolute values for stress than those of this study. It has been well established over many articles that stress parameter values are very sensitive to both the basic definition and the computation methodology (e.g., Atkinson and Beresnev, 1997; Allman and Shearer, 2007, 2009), and thus absolute values of the stress parameter can only be compared across studies if the definition of stress and method of computation
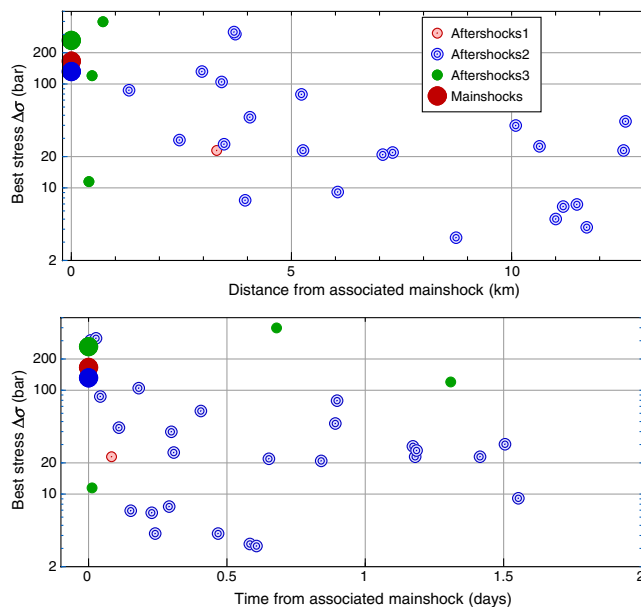
Figure 11. Stress parameter values as a function of (top) distance and (bottom) time from the associated mainshock. The large dots are the three mainshocks (in chronological order), whereas smaller dots show their aftershocks. The color version of this figure is available only in the electronic edition.

Figure 12. Attenuation of modified Mercalli intensity (MMI) with epicentral distance for the Prague mainshock events, in comparison to the intensity prediction equation (IPE) of Atkinson, Worden, and Wald (2014). Smaller symbols show actual reported MMI values while larger symbols with error bars show mean and standard deviation in distance bins 0.2 log units in width. The color version of this figure is available only in the electronic edition.

are consistent. There are significant differences in methods used to calculate stress between the two studies. In particular, Sumy *et al.* (unpublished manuscript, 2016; see Data and Resources) used a spectral fitting method that assumed a $1/R$ geometric spreading model, whereas the attenuation in this study is steeper ($1/R^{1.3}$ spreading per equation 9), and stress parameters are determined based on response spectral shape. Because of the strong trade-off between geometric spreading and stress parameter (Boore *et al.*, 2010; Yenier and Atkinson, 2014), it is not surprising that their stress parameters are systematically lower than those of this study. There are numerous other minor differences such as the form of equation used to convert corner frequency to stress and the treatment of site response terms. In this study, we ensure that the definition and methodology of determining stress is fully consistent with the way it is applied in GMPEs as described by Yenier and Atkinson (2015a,b). This allows us to focus on the implications of the results for the prediction of ground motion. By contrast, the Sun and Hartzell (2014) study focused on determination of the slip on the fault plane and did not evaluate ground-motion amplitudes.

The work of Hough (2014) focused on modified Mercalli intensity (MMI) observations and their decay with distance. She noted that at close epicentral distances the MMI values for induced events are consistent with those from natural earthquakes of the same magnitude, which is in qualitative agreement with the key result of this study. However, she also noted an apparent deficiency in observed MMI for induced events at large distances, in comparison to the intensity prediction equation (IPE) of Atkinson and Wald (2007). She interpreted the low regional values of MMI for
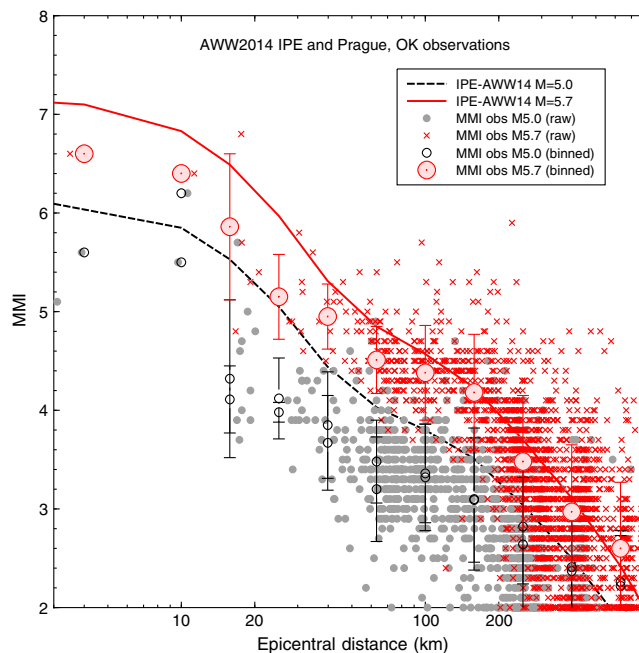
induced events as evidence for relatively low levels of high-frequency ground motion, in comparison to those for natural events of the same magnitude. The issue is illustrated in Figure 12, which plots the MMI values for the three mainshock events of this study in comparison to the IPE of Atkinson, Worden, and Wald (2014); the MMI observations include both the raw observations for each zip code, and mean values in distance bins, all from the Atkinson, Worden, and Wald (2014) database. This figure is very similar to plots made by Hough (2014) for the same events, except that we compare observations to the updated Atkinson, Worden, and Wald IPE, in preference to the older Atkinson and Wald (2007) IPE used by Hough. The updated IPE features somewhat faster MMI attenuation relative to Atkinson and Wald (2007). Overall, we concur with Hough that the MMI values are generally lower than would be expected for average natural events of the same magnitude. However, the differences are not as marked as those noted by Hough, due to our use of an updated IPE. For the largest event, the deficiency in observed MMI is not statistically compelling. For the **M** 5.0 events, the MMI values are clearly deficient in the 20–200 km distance range relative to the IPE. In our view, the observed differences are understandable when one considers the aspects of attenuation and source scaling that are not captured in generic IPEs. In particular, IPEs implicitly reflect the stress parameter and attenuation attributes for events of average focal depth ($d \approx 10$ km). Because induced events are
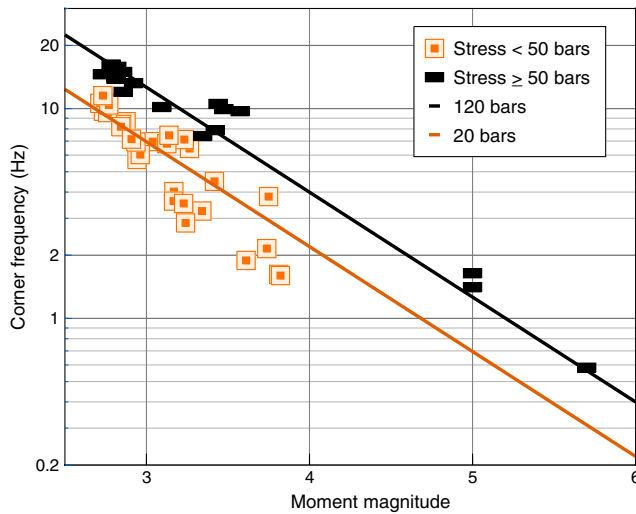
Figure 13. Scaling of corner frequency of events with moment magnitude (symbols), in comparison to lines showing constant-stress scaling for 20 and 120 bars. The color version of this figure is available only in the electronic edition.

shallow, their stress parameters are less than average for natural events of the same magnitude; this can be seen in Figure 8, which shows that the stress parameters for the three main-shock events studied here are less than average for natural events ($d \approx 10$ km) in CENA, simply because of their focal depth. Thus, we believe that the results of Hough (2014), and those shown in Figure 12, are consistent with the findings of this study. Specifically, the ground motions of induced events are comparable to those of natural events of the same magnitude and focal depth. However, if the ground motions of induced events are compared with those of deeper natural events, they will appear to be high at close distances and low at further distances, due to the effects of the shallow focal depth on source and attenuation scaling.

In Figure 13, we examine the scaling behavior of the corner frequency as a function of magnitude, in comparison to the scaling expected for constant stress. It is interesting that there is no significant deviation from the constant-stress slope. This is in accord with results for moderate-to-large events (e.g., Allmann and Shearer, 2009). Deviations from the constant-stress trend for events of **M** < 4.0 are seen in some regions (e.g., Mereu *et al.*, 2013), but not in others (e.g., Allmann and Shearer, 2007). There are different populations of stress values in Figure 13. We can group these, approximately, into a high-stress population having an average stress near 120 bars, and a low-stress population having a value near 20 bars. This is consistent with Figures 9–11, but demonstrates that the reason for the differing stress values does not relate to magnitude scaling. The events appear to follow the expected relationship for self-similar scaling, but there is a wide range of stress parameter values. A similar observation was made by Allmann and Shearer along the San Andreas fault, in which they observed high-stress values in the hypocentral region of the 2004 **M** 6.0 Parkfield earth-

quake, but lower stress values in the Middle Mountain asperity and along the creeping sections of the fault, while the constant-stress scaling was maintained.

Specification of Generic GMPE for Oklahoma Earthquakes

To define a GMPE for induced mainshock events in Oklahoma, we determine a regional calibration factor (ΔC_{OK}) that closes the amplitude gap between the CENA GMPE of YA15 for B/C site conditions and observed amplitudes in Oklahoma, generally on C sites. Thus, the Oklahoma GMPE for specified magnitude, distance, and stress parameter is given as

$$\ln Y_{\mathrm{OK},C} = F_M + F_{\Delta\sigma} + F_Z + \gamma_{\mathrm{CENA}} D_{\mathrm{rup}} + C_{\mathrm{CENA}} + \Delta C_{\mathrm{OK}}, \qquad (14)$$

in which $Y_{\mathrm{OK},C}$ represents the median ground-motion amplitude for average site conditions in Oklahoma (NEHRP C). Equation (14) is simply the CENA GMPE model of YA15 with an added constant term (ΔC_{OK}).

The regional calibration factor (ΔC_{OK}) reconciles the predicted and observed amplitudes, accounting for the overall differences between the CENA GMPE and the ground-motion database in Oklahoma. We determine the value of ΔC_{OK} based on the analysis of event-specific residuals, after removing the effects of all specified model parameters for Oklahoma.

$$\delta_{ij} = \ln Y_{\mathrm{OK},ij} - (F_{M,i} + F_{\Delta\sigma,i} + F_{Z,i,j} + \gamma_{\mathrm{CENA}} D_{\mathrm{rup},i,j} + F_{S,j} + C_{\mathrm{CENA}}), \qquad (15)$$

in which δ_{ij} represents the ground-motion residual for event i and station j, for a given ground-motion parameter. $F_{\Delta\sigma,i}$ is the stress adjustment factor (equation 4) evaluated for the $\Delta\sigma$ value of event i. Specifying the stress adjustment value for each event individually provides flexibility to accommodate the varying stress levels in time and space that were noted in the previous section. We will return to this issue later, with regard to how to handle this problem for future events with unknown stress. Figure 14 shows that there are no apparent trends in the mean event residuals ($\delta_i = \sum \delta_{ij}/n_i$, in which n_i is the number of records obtained from event i; $n_i \geq 3$ at a given period) with magnitude or depth. This indicates that the magnitude scaling of ground motions is well described by the F_M function. It is noteworthy that the mean event residuals show large variability, particularly for short periods. The δ_i values attain a standard deviation of ~0.58 ln units (factor of 1.8) for short periods ($T < 0.1$ s) and PGA. This decreases to ~0.36 ln units (factor of 1.4), for longer periods ($T > 0.5$ s). The Oklahoma calibration factor relative to the CENA GMPE (ΔC_{OK}) is determined as the average of δ_i values over all events. This factor includes the average site response for the stations relative to the B/C reference condition for the CENA model; thus it is not surprising that the ΔC_{OK} values, listed in Table 4, have positive values at all
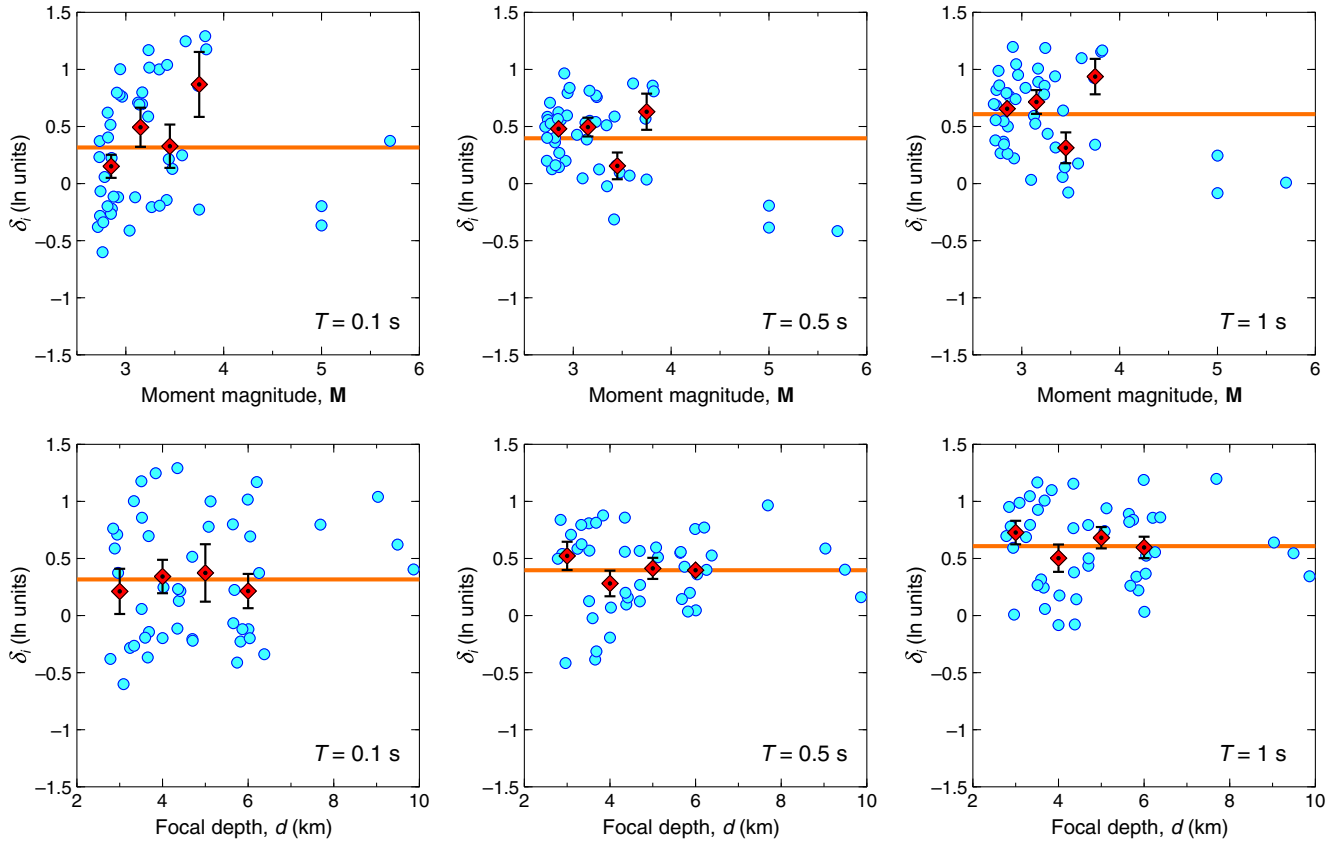
Figure 14.   Event residuals δ_i as a function of (top) magnitude and (bottom) depth, for different spectral periods. Diamonds show average δ_i determined for evenly spaced magnitude (0.3**M** in width) and depth (1 km in width) bins, and error bars represent the standard error about the mean. Horizontal line represents the average δ_i over all magnitudes and depths. The color version of this figure is available only in the electronic edition.

periods. Moreover, as shown in Figure 15, the ΔC_{OK} values increase with period at $T > 0.4$ s, which is also suggestive of site response for deeper deposits. Other factors contributing to the Oklahoma calibration may be regional attributes such as crustal properties, source mechanisms, and near-surface attenuation (κ_0 parameter).

We correct individual residuals for the average event residual (i.e., $\delta'_{ij} = \delta_{ij} - \delta_i$) to further assess the performance of the attenuation model parameters. Figure 16 shows the δ'_{ij} values as a function of rupture distance. The mean δ'_{ij} determined for log-spaced distance bins generally have near-zero values, indicating that the assumed CENA attenuation parameters are appropriate. However, the mean δ'_{ij} in the closest distance bin (3 km $< D_{rup} <$ 5 km) is positive, as shown in the figure, indicating a tendency for stronger-than-predicted motions very close to the epicenter. This discrepancy appears to be prominent for short-period motions and decreases with increasing period.

As discussed earlier, the mainshock events and the earthquakes that happen after the initial aftershock sequences subside have significantly higher stress parameters. This has important implications in terms of prediction of ground motions for seismic-hazard assessment. In Figure 17, we compare the site-corrected (NEHRP C) ground motions of

M ≥ 3.0 events to our proposed GMPE for Oklahoma (equation 14). Observed motions are plotted for different magnitude bins, which are categorized based on the event stress parameter. The predictions are evaluated at mid-magnitude for each bin, using the CENA stress parameter model (equation 12). A focal depth of 5 km is assumed, which is the average depth of the Prague events. For this depth, the predicted average stress for CENA events is 45 bars at **M** 3.0, increasing to 70 bars for **M** ≥ 5.0. Also shown in Figure 17 is the empirical GMPE developed by Atkinson (2015; hereafter, A15) based on **M** 3.0–6.0 events in California at hypocentral distances < 40 km; this GMPE has been proposed as a suitable proxy GMPE for induced events. For consistency with this study, the alternative effective-depth saturation term (which controls the rolloff of the curves at very close distances) was selected for the plot, though this choice does not matter for the purposes of this exercise. For consistency, the A15 model was converted from B/C to C using the calibration factor (ΔC_{OK}), which primarily represents average site response for stations relative to the B/C site condition. The A15 model and the model of this study are in reasonable agreement in overall amplitude level, but the model of this study has a more realistic attenuation shape for distances beyond 50 km. This is because our model includes the transition from direct-wave to surface-
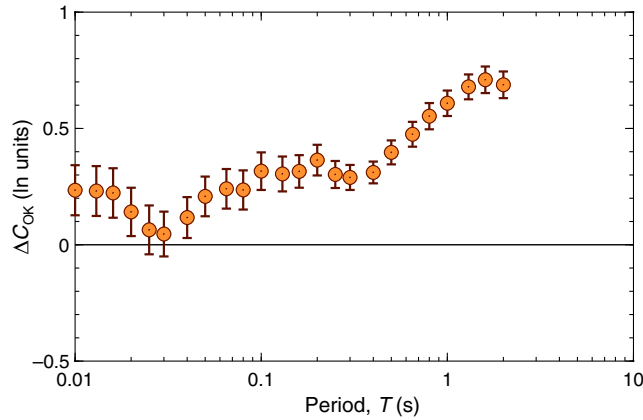
Figure 15. Empirical calibration factor for average Oklahoma sites (ΔC_{OK}, Table 4) relative to the CENA GMPE of YA15 (for B/C). Error bars represent the standard error about C_{OK}. The color version of this figure is available only in the electronic edition.

Table 4
Anelastic Attenuation Coefficient for Central and Eastern North America (CENA) (γ_{CENA}) and Oklahoma Calibration Factor (ΔC_{OK}) for Oklahoma

T (s)	γ_{CENA}	ΔC_{OK}
0.010	-4.661×10^{-3}	2.344×10^{-1}
0.013	-4.693×10^{-3}	2.310×10^{-1}
0.016	-4.687×10^{-3}	2.226×10^{-1}
0.020	-4.668×10^{-3}	1.413×10^{-1}
0.025	-4.884×10^{-3}	6.403×10^{-2}
0.030	-5.113×10^{-3}	4.616×10^{-2}
0.040	-5.266×10^{-3}	1.170×10^{-1}
0.050	-5.471×10^{-3}	2.079×10^{-1}
0.065	-5.714×10^{-3}	2.406×10^{-1}
0.080	-5.794×10^{-3}	2.357×10^{-1}
0.100	-5.640×10^{-3}	3.164×10^{-1}
0.130	-5.236×10^{-3}	3.044×10^{-1}
0.160	-4.771×10^{-3}	3.152×10^{-1}
0.200	-4.203×10^{-3}	3.639×10^{-1}
0.250	-3.648×10^{-3}	3.021×10^{-1}
0.300	-3.121×10^{-3}	2.894×10^{-1}
0.400	-2.438×10^{-3}	3.109×10^{-1}
0.500	-2.041×10^{-3}	3.971×10^{-1}
0.650	-1.638×10^{-3}	4.750×10^{-1}
0.800	-1.426×10^{-3}	5.527×10^{-1}
1.000	-1.259×10^{-3}	6.082×10^{-1}
1.300	-1.063×10^{-3}	6.788×10^{-1}
1.600	-1.171×10^{-3}	7.092×10^{-1}
2.000	-1.016×10^{-3}	6.876×10^{-1}
PGA	-4.667×10^{-3}	2.305×10^{-1}
PGV	-2.792×10^{-3}	3.067×10^{-1}

wave spreading at regional distances, whereas the A15 model focused on distances <50 km. At distances <50 km, the two models are in good agreement for periods of 0.5 s and greater, except that the A15 model results in larger amplitudes (by about a factor of 2) at very close distances. The observations do not allow discrimination of which model is preferred at such distances. For short periods (0.1 s), PGA and PGV, our model predicts higher amplitudes than does the A15 model. This is expected because it features a higher stress parameter than that for California events. The data plotted in Figure 17 suggest that a higher stress parameter is warranted for induced Oklahoma events, when one excludes the lower-stress aftershocks ($\Delta\sigma < 30$ bar). On the flip side, the A15 model provides a good agreement with observed motions from many of the lower-stress Oklahoma events. We should acknowledge that our model underpredicts the short-period (0.1 s) motions, PGA and PGV for high-stress **M** 3.4–3.7 events (filled circles in Fig. 17) by more than a factor of 2. This is because these events all had very high stress parameters (126, 302, 316, and 398 bars), much higher than the average for such events in the CENA model (51 bars).

A key question in applying the proposed GMPE for future Oklahoma events concerns the value of stress parameter that should be applied. As shown in Figure 17, the ground motions of mainshock events and many of the higher-stress following events are consistent with stress parameters observed for shallow (<10 km) natural events in CENA, whereas, in contrast, the ground motions of low-stress aftershocks are more consistent with the stress parameter level implied by the A15 model. We conclude that the CENA stress parameter model is appropriate for moderate-to-large induced mainshock events in Oklahoma. However, it is important to recognize that the stress parameter for induced events is highly dependent on focal depth, and even for a known focal depth it has a standard deviation of about a factor of 3 (Fig. 8). The variability in stress parameter maps into an interevent aleatory uncertainty of about a factor of 2 in high-frequency ground motions, per

equation (4) (for a known focal depth). The variability of the stress parameter, and hence ground motion, further increases when aftershocks are considered due to their space- and time-dependent source attributes.

Recall that we determined stress parameters based on the observed spectral shape, and the overall amplitude differences (δ_i, Fig. 14) were modeled by the regional calibration factor ΔC_{OK}. This factor primarily corresponds to the average site response relative to the B/C site condition. However, it may also be influenced by regional attributes such as crustal properties, source mechanisms, near-surface attenuation (κ_0 parameter), and ground-motion duration relative to the CENA model. Uncertainty in the ΔC_{OK} values may include components of both inter- and intraevent uncertainty as well as epistemic uncertainty in the applicability of the adopted CENA model. Decoupling these uncertainties is not feasible with limited data of this study. Instead, all these factors can be considered to influence the total aleatory uncertainty in hazard calculations.

Considering just the mainshock events and the events that follow the aftershock sequences (more than 1 week after the third event), the total aleatory variability of ground motions is 0.52, 0.54, 0.52, 0.43, 0.42, and 0.43 ln units at periods 0.05, 0.1, 0.2, 0.5, 1, and 2 s, respectively. These values are generally smaller than the total aleatory variability of natural events in CENA (1.13, 1.01, 0.85, 0.77, 0.75, and 0.73 ln units, respectively), particularly because ground motions
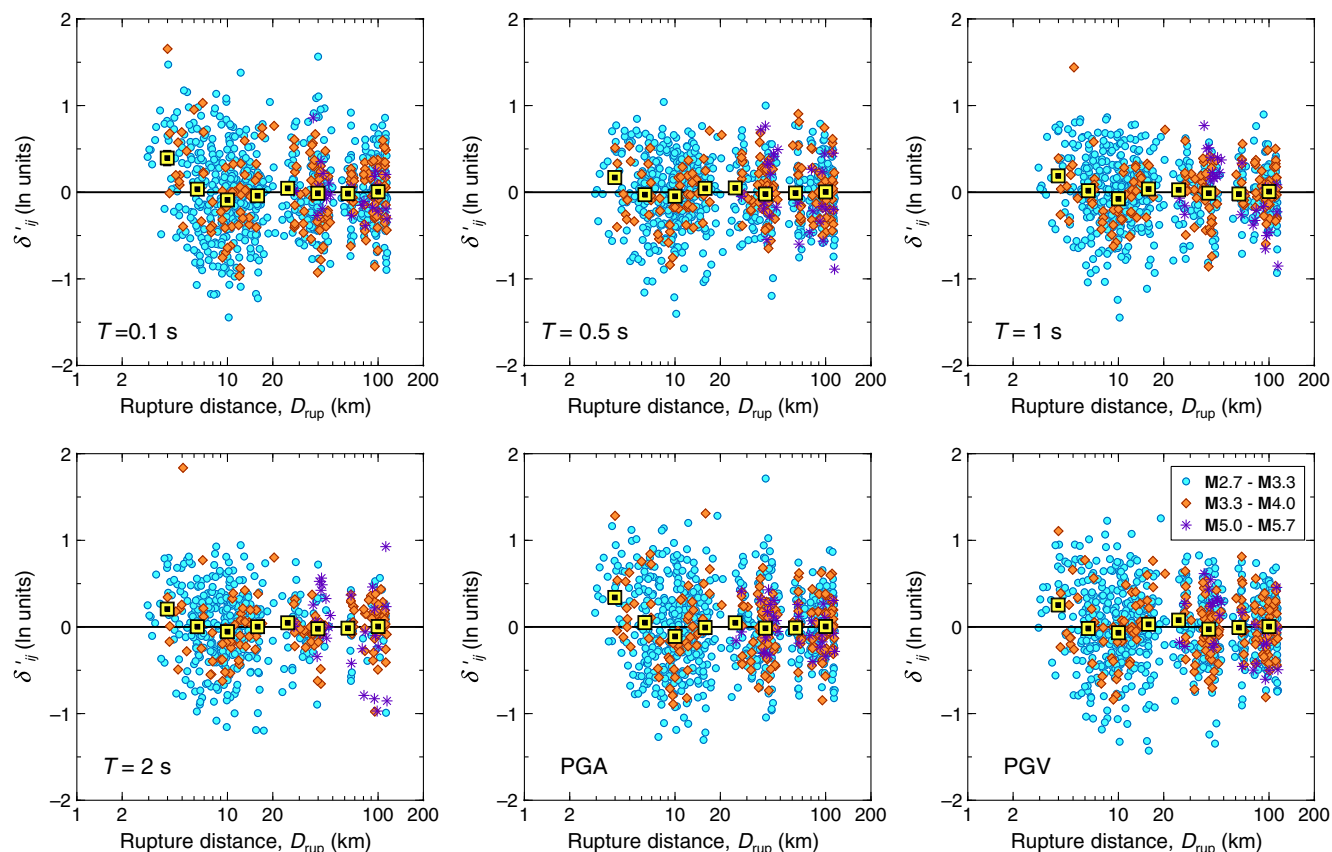
Figure 16.   Event-corrected residuals (δ'_{ij}) as a function of distance, for different magnitude bins. The residuals for the three $\mathbf{M} \geq 5$ mainshocks are shown as asterisks. Squares indicate the mean δ'_{ij} values determined for distance bins of 0.2 log-unit intervals, over all magnitudes. Standard errors of mean δ'_{ij} values are smaller than the square symbol size. The color version of this figure is available only in the electronic edition.

of this study represent variations of source, attenuation, and site attributes within a relatively small region in Oklahoma, whereas ground motions of natural CENA events represent variability of such effects over a much wider area.

There is significant epistemic uncertainty in the ground motions from Oklahoma events remaining following this study, because we studied a single sequence with limited magnitude distribution. The applicability of these findings to other sequences must await further analysis with larger datasets including a broader range of source attributes. Similarly, the data from this study are too limited to enable an objective evaluation of the epistemic uncertainty in GMPEs for induced events. This topic will be the subject of future work with additional data.

Summary and Conclusion

Prediction of ground motions that may be produced by induced earthquakes in Oklahoma is important for the assessment of hazard contributions from induced seismicity. In this study, we develop a ground-motion model using observations from the 2011 Prague sequence. The method is based on modifying the key model parameters of a regionally adjustable generic GMPE that was derived from simulations calibrated to the California ground-motion database. The Oklahoma GMPE is calibrated to capture the observed source and attenuation attributes of induced events. Because of the combined use of regional observations and seismological modeling, it is applicable over a broad range of magnitudes (**M** 3–6) and distances (3–150 km). We show that ground-motion attenuation in Oklahoma agrees well with the observed decay rates in a wider region of CENA.

The stress parameter values for the induced Prague sequence, controlling the strength of high-frequency radiation, decay sharply with time in the first few days following the largest events of the sequence, then gradually recover. The mainshock events, and the events following the initial aftershock decay sequences, have stress parameters consistent with those for natural earthquakes of similar magnitude and depth in CENA. Because of the relatively high-stress parameters in CENA, the events produce high-frequency ground motions that are larger than expected for shallow natural events in California, which are characterized by lower stress. An oft-heard statement to the effect that induced events have low-stress drops and therefore produce low ground motions is not borne out by ground-motion recordings for moderately induced mainshock events at close distances.
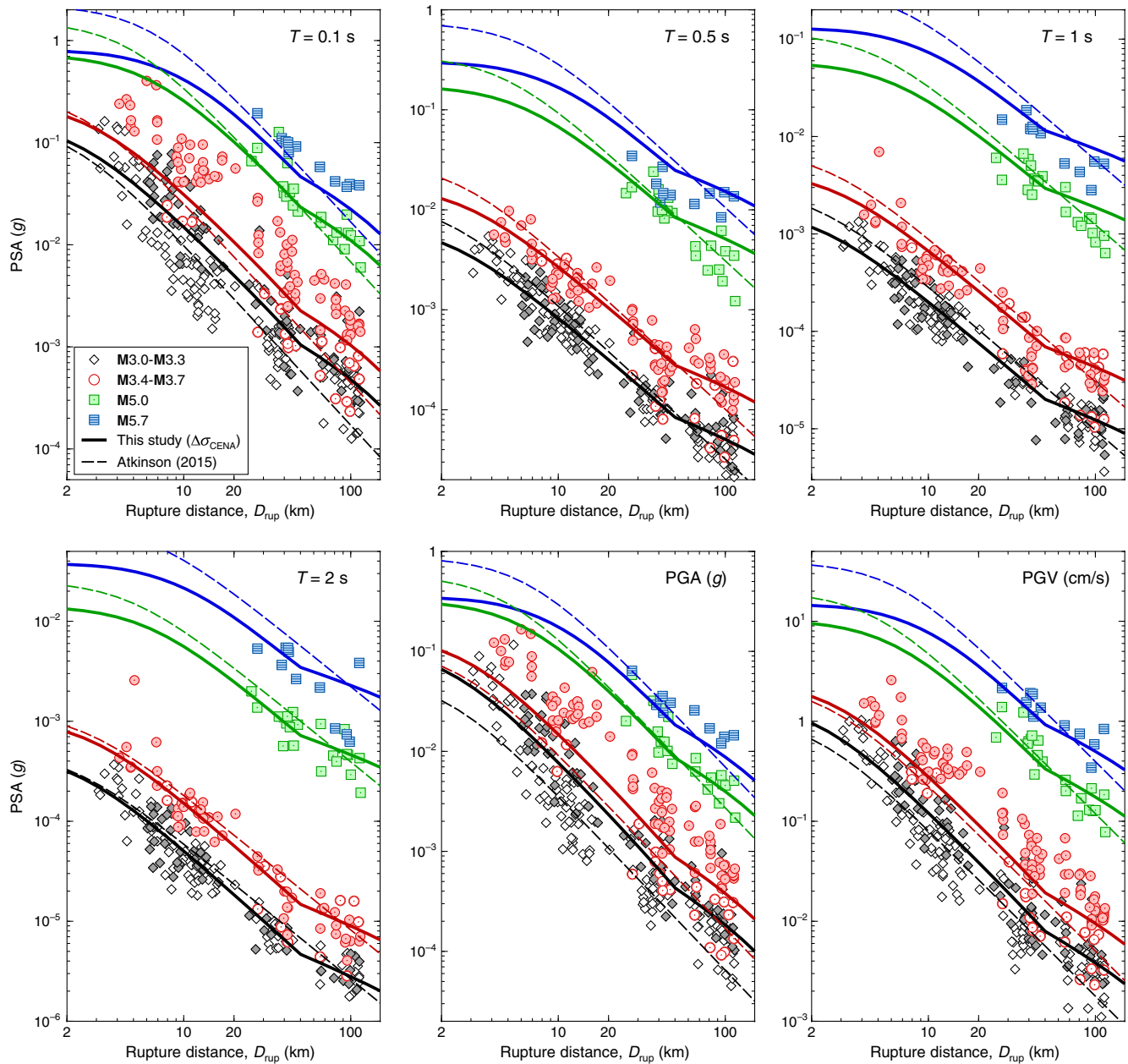
Figure 17. Ground motions of the Prague sequence in comparison to the derived GMPE (equation 14 with CENA stress model), for average National Earthquake Hazards Reduction Program (NEHRP) C site condition. Observed motions are grouped as low-stress events ($\Delta\sigma < 30$ bar, open symbols) and high-stress events ($\Delta\sigma > 30$ bar, filled symbols). All three mainshocks ($\mathbf{M} \geq 5.0$) attain high-stress parameters. The Atkinson (2015) predictive model is also plotted, after adjusting for Oklahoma by adding the conversion from NEHRP B/C to C. The color version of this figure is available only in the electronic edition.

Data and Resources

The ground-motion database for this study comprises processed seismograms from a dense, local seismic array data deployed by the U.S. Geological Survey (USGS) and the University of Oklahoma, as described by Sumy *et al.* (2014). The unpublished manuscript by D. Sumy, C. Neighbors, E. Cochran, and K. Keranen (2016) is "Low stress drops observed for aftershocks of the 2011 M_{w} 5.6 Prague Oklahoma earthquake" has been submitted to *J. Geophys. Res.* The magnitude values used here are from the Global Centroid Moment Tensor (CMT) catalog (www.globalcmt.org; last accessed February 2016). Regression analyses are performed using MATLAB software (https://www.mathworks.com/products/matlab, last accessed February 2016). All figures, except Figure 1, were produced using CoPlot software. Figure 1 was generated using QGIS software.

Acknowledgments

and three anonymous reviewers for valuable suggestions that improved the clarity of the article.

References

Allen, T. I., and D. J. Wald (2007). Topographic slope as a proxy for seismic site conditions (V_{S30}) and amplification around the globe, *U.S. Geol. Surv. Open-File Rept. 2007-1357*, 69 pp.

Allen, T. I., and D. J. Wald (2009). On the use of high-resolution topographic data as a proxy for seismic site conditions (V_{S30}), *Bull. Seismol. Soc. Am.* **99,** 935–943.

Allmann, B., and P. Shearer (2007). Spatial and temporal stress drop variations in small earthquakes near Parkfield, California, *J. Geophys. Res.* **112,** no. B04305, doi: 10.1029/2006JB004395.

Allmann, B., and P. Shearer (2009). Global variations of stress drop for moderate to large earthquakes, *J. Geophys. Res.* **114,** no. B01310, doi: 10.1029/2008JB005821.

Atkinson, G. M. (2015). Ground-motion prediction equation for small-to-moderate events at short hypocentral distances, with application to induced-seismicity hazards, *Bull. Seismol. Soc. Am.* **105,** 981–992.

Atkinson, G. M., and I. Beresnev (1997). Don't call it stress drop, *Seismol. Res. Lett.* **68,** 3–4.

Atkinson, G. M., and D. M. Boore (2014). The attenuation of Fourier amplitudes for rock sites in eastern North America, *Bull. Seismol. Soc. Am.* **104,** 513–528.

Atkinson, G. M., and D. Wald (2007). Modified Mercalli intensity: A surprisingly good measure of ground motion, *Seismol. Res. Lett.* **78,** 362–368.

Atkinson, G. M., H. Ghofrani, and K. Assatourians (2015). Impact of induced seismicity on the evaluation of seismic hazard: Some preliminary considerations, *Seismol. Res. Lett.* **86,** 1116–1124.

Atkinson, G. M., D. W. Greig, and E. Yenier (2014). Estimation of moment magnitude (M) for small events (M <4) on local networks, *Seismol. Res. Lett.* **85,** 1116–1124.

Atkinson, G. M., B. Hassani, A. Singh, E. Yenier, and K. Assatourians (2015). Estimation of moment magnitude and stress parameter from ShakeMap ground-motion parameters, *Bull. Seismol. Soc. Am.* **105,** 2572–2588.

Atkinson, G., B. Worden, and D. Wald (2014). Intensity prediction equations for North America, *Bull. Seismol. Soc. Am.* **104,** 3084–3093.

Babaie Mahani, A., and G. M. Atkinson (2012). Evaluation of functional forms for the attenuation of small-to-moderate-earthquake response spectral amplitudes in North America, *Bull. Seismol. Soc. Am.* **102,** 2714–2726.

Boore, D. M. (2003). Simulation of ground motion using the stochastic method, *Pure Appl. Geophys.* **160,** 635–676.

Boore, D. M. (2009). Comparing stochastic point-source and finite-source ground motion simulations: SMSIM and EXSIM, *Bull. Seismol. Soc. Am.* **99,** 3202–3216.

Boore, D. M., K. Campbell, and G. Atkinson (2010). Determination of stress parameters for eight well-recorded earthquakes in eastern North America, *Bull. Seismol. Soc. Am.* **100,** 1632–1645.

Boore, D. M., J. P. Stewart, E. Seyhan, and G. M. Atkinson (2014). NGA-West2 equations for predicting response spectral accelerations for shallow crustal earthquakes, *Earthq. Spectra* **30,** 1057–1085.

Brown, S., and R. Bruhn (1998). Fluid permeability of deformable fracture networks, *J. Geophys. Res.* **103,** 2489–2500.

Brune, J. N. (1970). Tectonic stress and the spectra of seismic shear waves from earthquakes, *J. Geophys. Res.* **75,** 4997–5009.

Ellsworth, W. (2013). Injection-induced earthquakes, *Science* **341,** no. 6142, doi: 10.1126/science.1225942.

Herrmann, R., H. Su, and H. Guo (2015). The earthquake process in Oklahoma. Search and Discovery Article #80497, AAPG Datapages, *presented at AAPG Mid-Continent Section Meeting*, 4–6 October 2015, Tulsa, Oklahoma.

Holland, A. A. (2015). Preliminary fault map of Oklahoma, *Okla. Geol. Surv. Open-File Rept. OF3-2015*, 1.

Hough, S. (2014). Shaking from injection-induced earthquakes in the central and eastern United States, *Bull. Seismol. Soc. Am.* **104,** 2619–2626.

Keranen, K., H. Savage, G. Abers, and E. Cochran (2013). Potential induced earthquakes in Oklahoma, USA: Links between wastewater injection and the 2011 M_w 5.7 earthquake sequence, *Geology* **41,** 699–702.

Llenos, A. L., and A. J. Michael (2013). Modeling earthquake rate changes in Oklahoma and Arkansas: Possible signatures of induced seismicity, *Bull. Seismol. Soc. Am.* **103,** 2850–2861.

McNamara, D. E., H. M. Benz, R. B. Herrmann, E. A. Bergman, P. Earle, A. Holland, R. Baldwin, and A. Gassner (2015). Earthquake hypocenters and focal mechanisms in central Oklahoma reveal a complex system of reactivated subsurface strike-slip faulting, *Geophys. Res. Lett.* **42,** 2742–2749.

Mereu, R., S. Dineva, and G. Atkinson (2013). The application of velocity spectral stacking to extract information on source and path effects for small-to-moderate earthquakes in southern Ontario with evidence for constant width faulting, *Seismol. Res. Lett.* **84,** 899–916.

National Earthquake Hazards Reduction Program (NEHRP) (2000). NEHRP Recommended Provisions for Seismic Regulations for New Buildings and Other Structures (FEMA 368), Part 1: Provisions, Federal Emergency Management Agency, Washington, D.C, 39–40.

Novakovic, M., and G. M. Atkinson (2015). Preliminary evaluation of ground motions from earthquakes in Alberta, *Seismol. Res. Lett.* **86,** 1086–1095.

Petersen, M. D., C. S. Mueller, M. P. Moschetti, S. M. Hoover, J. L. Rubinstein, A. L. Llenos, A. J. Michael, W. L. Ellsworth, A. F. McGarr, A. A. Holland, *et al.* (2015). Incorporating induced seismicity in the 2014 United States National Seismic Hazard Model—Results of 2014 workshop and sensitivity studies, *U.S. Geol. Surv. Open-File Rept. 2015–1070*, 75 pp.

Rogers, A. M., and D. M. Perkins (1996). Monte Carlo simulation of peak acceleration attenuation using a finite-fault uniform-patch model including isochron and extremal characteristics, *Bull. Seismol. Soc. Am.* **86,** 79–92.

Sumy, D., E. Cochran, K. Keranen, M. Wei, and G. Abers (2014). Observations of static Coulomb stress triggering of the November 2011 M 5.7 Oklahoma earthquake sequence, *J. Geophys. Res.* **119,** 1904–1923.

Sun, X., and S. Hartzell (2014). Finite-fault slip model of the 2011 M_w 5.6 Prague, Oklahoma earthquake from regional waveforms, *Geophys. Res. Lett.*, doi: 10.1002/2014GL060410.

Yenier, E., and G. M. Atkinson (2014). Equivalent point-source modeling of moderate-to-large magnitude earthquakes and associated ground-motion saturation effects, *Bull. Seismol. Soc. Am.* **104,** 1458–1478.

Yenier, E., and G. M. Atkinson (2015a). An equivalent point-source model for stochastic simulation of earthquake ground motions in California, *Bull. Seismol. Soc. Am.* **105,** 1435–1455.

Yenier, E., and G. M. Atkinson (2015b). Regionally adjustable generic ground-motion prediction equation based on equivalent point-source simulations: Application to central and eastern North America, *Bull. Seismol. Soc. Am.* **105,** 1989–2009.

Department of Earth Sciences
Western University
London, Ontario
Canada N6A 5B7
emrah.yenier@gmail.com
gmatkinson@aol.com
    (E.Y., G.M.A.)

Incorporated Research Institutions for Seismology
1200 New York Avenue, NW Suite 400
Washington, D.C. 20005
sumy@iris.edu
    (D.F.S.)